





ARTICLE

TRAIL signaling promotes entosis in colorectal cancer

Emir Bozkurt^{1,2} , Heiko Düssmann¹ , Manuela Salvucci¹, Brenton L. Cavanagh³ , Sandra Van Schaeysbroeck⁴, Daniel B. Longley⁴, Seamus J. Martin⁵, and Jochen H.M. Prehn¹ 

Entosis is a form of nonphagocytic cell-in-cell (CIC) interaction where a living cell enters into another. Tumors show evidence of entosis; however, factors controlling entosis remain to be elucidated. Here, we find that besides inducing apoptosis, TRAIL signaling is a potent activator of entosis in colon cancer cells. Initiation of both apoptosis and entosis requires TRAIL receptors DR4 and DR5; however, induction of apoptosis and entosis diverges at caspase-8 as its structural presence is sufficient for induction of entosis but not apoptosis. Although apoptosis and entosis are morphologically and biochemically distinct, knockout of *Bax* and *Bak*, or inhibition of caspases, also inhibits entotic cell death and promotes survival and release of inner cells. Analysis of colorectal cancer tumors reveals a significant association between TRAIL signaling and CIC structures. Finally, the presence of CIC structures in the invasive front regions of colorectal tumors shows a strong correlation with adverse patient prognosis.

Introduction

Cell death is essential for maintenance of homeostasis in multicellular organisms. Studies over the last decade have revealed that cell death occurs as a result of simultaneous activation of multiple interconnected pathways. Apoptosis is a form of controlled cell death associated with distinct morphological changes, such as membrane blebbing, nuclear condensation, and fragmentation (Kerr et al., 1972). Apoptosis is triggered through a family of cysteine proteases known as caspases. Depending on how caspases are activated, apoptosis can be induced by the intrinsic and extrinsic pathways. The intrinsic pathway involves permeabilization of the mitochondrial outer membrane (MOMP) by Bax and Bak, resulting in release of mitochondrial intermembrane proteins leading to activation of caspase-9 and executioner caspases-3, -6, and -7. Initiation of the extrinsic pathway requires binding of specific death ligands to transmembrane receptors to initiate the formation of death-inducing signaling complex, ultimately resulting in caspase-8 activation. Caspase-8 can then trigger a downstream apoptotic cascade either by directly activating the effector caspases or engaging with the mitochondrial pathway by cleaving BID, which leads to MOMP and further activation of executioner caspases (Green, 2011).

TNF-related apoptosis-inducing ligand (TRAIL) is a type II transmembrane protein mainly expressed on the surface of a

variety of normal cells (Wiley et al., 1995) as well as most immune cells (de Loeff et al., 2019; Schaefer et al., 2007). Both membrane-bound and soluble TRAIL can bind to its death domain-containing receptors (DRs; TRAIL-R1/DR4 and TRAIL-R2/DR5) on cancer cells to initiate apoptosis by activating the extrinsic pathway (Schaefer et al., 2007). Because DR4 and DR5 are frequently overexpressed in many cancers compared with normal tissues, targeting these receptors therapeutically has attracted much interest (de Miguel et al., 2016). However, first-generation agents failed in clinical trials, leading to the need to reevaluate TRAIL signaling from different perspectives, one of which focuses on understanding the nature of cancer cells that survive in response to TRAIL treatment (Fulda, 2013). When cancer cells are exposed to TRAIL, even at high TRAIL levels assumed to saturate all its receptors, only a fraction of cells undergo complete cell death (Roux et al., 2015). Accumulating evidence has suggested that this behavior arises from the parallel activation of cell survival pathways (Falschlehner et al., 2007). Indeed, although activation of TRAIL signaling recruits proteins such as FADD for apoptosis induction, binding of other regulators such as cellular FLICE-like inhibitory protein (c-FLIP) can switch the pathway toward the activation of survival signaling and generation of cytokines that may promote tumor growth (Hartwig et al., 2017; Henry and Martin, 2017).

¹Department of Physiology and Medical Physics, Centre for Systems Medicine, Royal College of Surgeons in Ireland, Dublin, Ireland; ²Department of Genetics and Bioengineering, Faculty of Engineering, Izmir University of Economics, Balçova, Izmir, Turkey; ³Cellular and Molecular Imaging Core, Royal College of Surgeons in Ireland, Dublin, Ireland; ⁴Centre for Cancer Research and Cell Biology, School of Medicine, Dentistry and Biomedical Sciences, Queen's University Belfast, Belfast, UK; ⁵Molecular Cell Biology Laboratory, Department of Genetics, The Smurfit Institute, Trinity College, Dublin, Ireland.

Correspondence to Jochen H.M. Prehn: jprehn@rcsi.ie.

© 2021 Bozkurt et al. This article is distributed under the terms of an Attribution–Noncommercial–Share Alike–No Mirror Sites license for the first six months after the publication date (see <http://www.rupress.org/terms/>). After six months it is available under a Creative Commons License (Attribution–Noncommercial–Share Alike 4.0 International license, as described at <https://creativecommons.org/licenses/by-nc-sa/4.0/>).

The phenomenon of cell-in-cell (CIC) structures has been reported for more than a century (Overholtzer and Brugge, 2008) and used as an umbrella term to describe any type of CIC interaction. However, it was only recently discovered that not all CIC structures are formed by phagocytosis-like activity. Entosis is a homotypic CIC invasion process by which one living cell (“inner cell”) actively enters another (nonphagocytic) living cell (“outer cell”) of the same type in a Rho/Rho-associated kinase (ROCK) signaling-dependent manner (Overholtzer et al., 2007). Inner cells are initially alive after invasion into another cell, can undergo cell division inside the outer cell, or can be released. However, the majority of inner cells undergo degradation inside outer cells by an autophagic lipidation-dependent lysosomal cell death mechanism known as entotic cell death (Florey et al., 2011). Remarkably, even though entotic cell death can result in elimination of cells at the individual level, entosis can confer a survival advantage to the outer cells under stress conditions (Hamann et al., 2017; Sun et al., 2014). The presence of TP53 (Mackay et al., 2018) and KRAS (Sun et al., 2014) mutations increase the likelihood of cancer cells undergoing entosis. Several human malignancies, including lung, head and neck, breast, colon, stomach, liver, and cervical cancers and melanoma, show evidence of CIC structures (Durgan et al., 2017; Overholtzer et al., 2007; Schenker et al., 2017; Mackay et al., 2018); however, the clinical relevance of CIC structures remains to be elucidated.

Here, while analyzing cell-to-cell variability during TRAIL-mediated caspase activation of colorectal cancer (CRC) cells at the single-cell level by time-lapse imaging, we discovered that in addition to induction of apoptosis, TRAIL signaling activates entosis in a proportion of colon cancer cells. We demonstrate that induction of entosis by TRAIL requires death receptors and structural presence of caspase-8 and contributes to survival of outer cells. On the other hand, inhibition of apoptosis signaling downstream of caspase-8 alters the fate of inner cells toward release. Furthermore, we demonstrate that the presence of CIC structures in CRC patients correlates with key components of the TRAIL signaling pathway, and the presence of CIC structures in the invading margins of tumors is an independent prognostic marker of disease recurrence for stage 3 CRC.

Results

Single-cell time-lapse microscopy reveals simultaneous induction of entosis and apoptosis upon TRAIL stimulation

We measured the kinetics of caspase activation by single-cell time-lapse microscopy in HCT116 colon cancer cells stably expressing a CFP-IETD-Venus fluorescent protein (Venus) fluorescence resonance energy transfer (FRET) probe, a fluorescent-based caspase activation reporter that can detect caspase-8-like and caspase-3-like activity during activation of apoptosis (Hellwig et al., 2008). Cells were also incubated with tetramethylrhodamine methyl ester (TMRM) to measure the time of MOMP during apoptosis (Fig. 1, A and B). We quantified the changes in CFP/FRET emission ratio in control cells as well as in response to TRAIL with or without cycloheximide (CHX). Translation inhibition by CHX downregulates key survival components during death receptor activation, such as c-FLIP, MCL-1, and BCL-XL, and is routinely

used to sensitize cells to TRAIL-induced apoptosis (van Dijk et al., 2013; Wajant et al., 2000; Guseva et al., 2008). Typically, cells responding to TRAIL/CHX exhibit a moderate increase in CFP/FRET emission ratio, indicating activation of caspase-8, followed by a drop in TMRM intensity as an indicator of MOMP and then a sharp increase in CFP/FRET ratio, indicating the activation of caspase-3 and other executioner caspases (Fig. 1 A; Hellwig et al., 2008; Roux et al., 2015). We did not observe any changes in CFP/FRET emission ratio in control cells (data not shown). In line with previous reports (Flusberg et al., 2013; Roux et al., 2015), HCT116 cells exhibited a heterogeneous response in IETD substrate cleavage in response to TRAIL. A proportion of cells showed IETD substrate cleavage followed by loss of TMRM intensity, which ultimately led to membrane blebbing and cell shrinkage, again indicating that apoptosis was induced. Other cells exhibited a slow substrate cleavage and retained intact morphology and TMRM staining, suggesting that these cells survived TRAIL treatment (Fig. 1, C and G). Overall, the omission of the protein synthesis inhibitor CHX yielded more heterogeneous IETD substrate cleavage compared with TRAIL and CHX treatment (Fig. 1, C and D).

While investigating cell-to-cell variability in caspase activation dynamics upon TRAIL stimulation, we noticed that a proportion of cells entered into neighboring cells and appeared inside a large vacuolar structure (Fig. 1, E–H; and Video 1). In separate time-lapse experiments, vacuolar structures showed LysoTracker accumulation, and inner cells in such structures underwent degradation, indicating that inner cells were degraded inside of acidic structures (Fig. S1, A and B; and Videos 2 and 3). We also observed occasions of not only single cells but also multiple cells invading into their neighbors. A period of time after CIC invasion, the majority of inner cells showed a reduction in the intensity of Venus, which is quenched at acidic pH (Shinoda et al., 2018). Remarkably, coincident with the reduction in Venus intensity, these cells exhibited a significant increase in the TMRM signal (Fig. 1, E–H, entotic 1 and 2). To further examine whether this increase was associated with inner cell death, we performed time-lapse microscopy to simultaneously measure fluorescence intensities of Venus, TMRM, and LysoTracker. We found that the reduction in Venus and the increase in TMRM fluorescence coincided with the accumulation of LysoTracker in inner cells that underwent degradation (Fig. S1 C and Video 4). Treatment with carbonyl cyanide-p-trifluoromethoxyphenylhydrazone (FCCP), a protonophore that dissipates the mitochondrial membrane potential, showed an immediate drop in TMRM intensity in outer and neighboring cells; however, inner cells undergoing degradation did not show a drop in TMRM fluorescence intensity, suggesting that the increase in TMRM fluorescence intensity was not related to changes in the mitochondrial membrane potential (Fig. S1 D). Interestingly, reduction in Venus and accumulation of TMRM and LysoTracker occurred only when inner cells underwent degradation. In rare cases, inner cells were released hours after CIC invasion (Fig. 1 H, entotic 3). There was no change in Venus, TMRM, and LysoTracker fluorescence intensities when inner cells were released (Fig. S1 C).

To examine the associations among entosis, entotic cell death, and IETD substrate cleavage upon TRAIL stimulation, we quantified

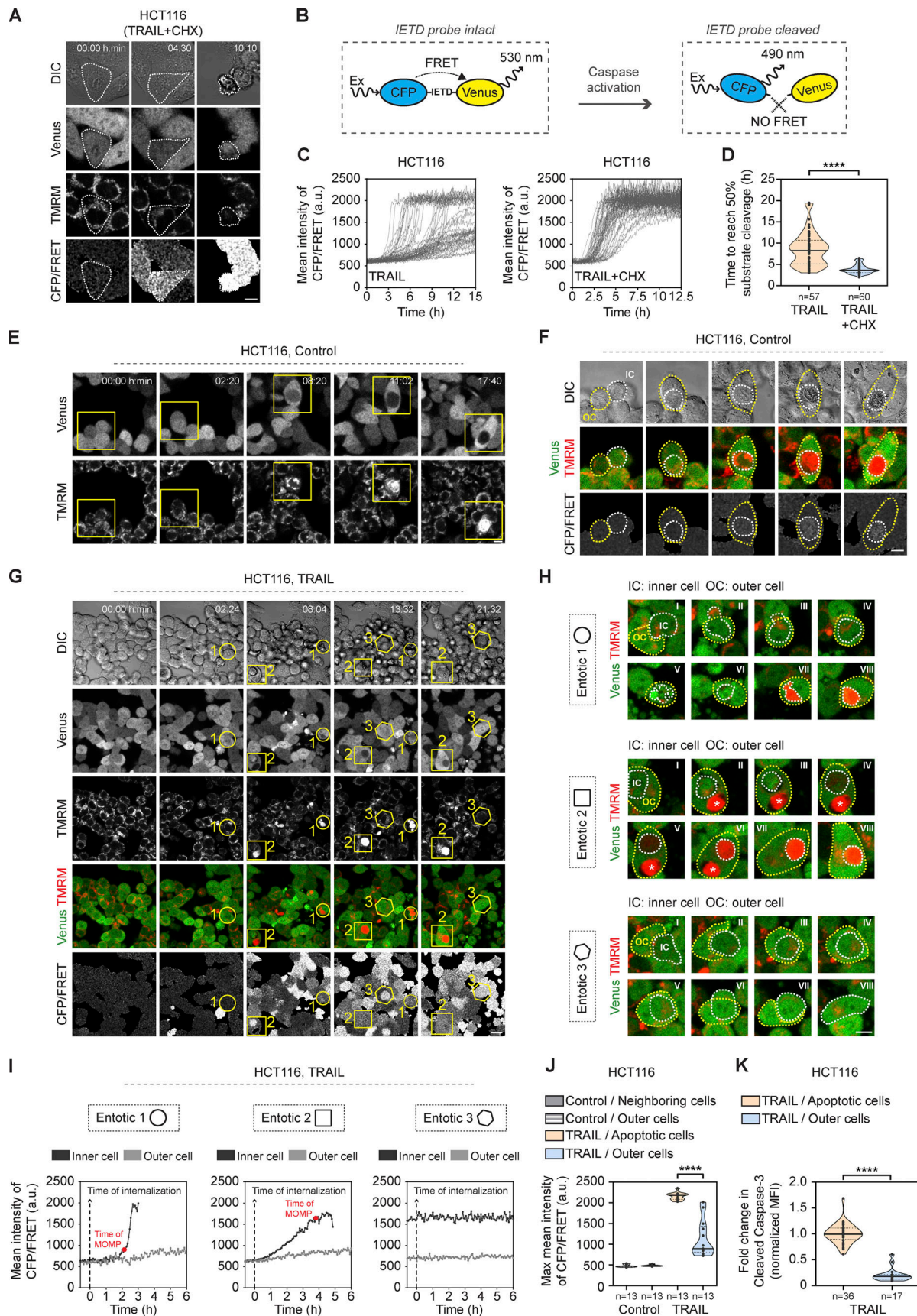


Figure 1. **Single-cell time-lapse microscopy reveals simultaneous induction of entosis and apoptosis upon TRAIL stimulation.** (A–D) HCT116 cells exhibit heterogeneity in caspase activation kinetics in response to TRAIL but not TRAIL + CHX. (A) Representative time-lapse images of HCT116 cells stably

expressing IETD-FRET probe treated with TRAIL + CHX. Venus, TMRM, and CFP/FRET emission ratio images are shown. Depicted area highlights an apoptotic cell. Scale bar: 20 μm . **(B)** Schematic representation of the intact (left) and the cleaved (right) forms of IETD-FRET probe. Ex is the excitation wavelength; see Materials and Methods for details. **(C)** Quantification of single-cell CFP/FRET emission ratio traces in response to TRAIL ($n = 57$, left) and TRAIL + CHX ($n = 60$, right). **(D)** Single-cell IETD substrate cleavage kinetics in response to TRAIL and TRAIL + CHX. Data are shown as individual values for each cell as well as median and quartiles from three experiments. ****, $P < 0.0001$ by unpaired two-tailed t test. **(E–H)** Live cell TMRM staining accumulates in inner cells during entotic cell death. Representative time-lapse images of control (E and F) and TRAIL-treated (G and H) HCT116 IETD showing formation of entotic structures. DIC, Venus (green), TMRM (red), and CFP/FRET emission ratio images are shown. Representative entosis events are highlighted in a circle (entotic 1), a square (entotic 2), and a hexagon (entotic 3). Scale bar: 20 μm . Combined Venus (green) and TMRM (red) images highlighting stages of depicted entosis events (H). White-dashed and yellow-dashed lines indicate inner cells and outer cells, respectively. White asterisk indicates another entotic event in an outer cell of interest. Entotic 1, inner cell shows apoptotic features, then undergoes entotic cell death; entotic 2, inner cell shows caspase activation and loss of TMRM signal, then undergoes entotic cell death; entotic 3, inner cell with caspase activation invades into another cell, then is released. Scale bar: 20 μm . **(I–K)** Outer cells exhibit slow caspase activation kinetics and show less cleaved caspase-3 levels in TRAIL treatment. **(I)** Quantification of CFP/FRET emission ratio traces of inner (black) and outer (gray) cells in entotic 1, entotic 2, and entotic 3. Dashed line with arrow indicates time of internalization. Red dot on the single-cell trace of interest represents time of TMRM intensity loss. **(J)** Quantification of maximum mean values of CFP/FRET emission ratio traces in outer cells, apoptotic cells, or neighboring cells in HCT116 treated with or without TRAIL. Single-cell CFP/FRET emission ratio traces of $n = 52$ cells (13 cells/group) were generated over 20 h of time-lapse microscopy, and the maximum value in each trace was recorded. Data are shown as individual values for each cell as well as median and quartiles from three experiments. ****, $P < 0.0001$ by one-way ANOVA followed by Tukey's multiple comparison test. **(K)** Quantification of immunofluorescence staining of cleaved caspase-3 (Asp175) levels in apoptotic cells ($n = 36$) and outer cells ($n = 30$) in HCT116 treated with TRAIL. Entosis events were characterized using 3D confocal microscopy images of DIC and Hoechst by detecting a round-shaped Hoechst-stained cell inside a vacuolar structure within another Hoechst-stained cell showing a crescent-shaped nuclear morphology. Cells showing fragmented nuclei and increased cleaved caspase-3 intensity were considered apoptotic. Data are shown as individual values for each cell as well as median and quartiles from three experiments. ****, $P < 0.0001$ by unpaired two-tailed t test. MFI, mean fluorescence intensity.

CFP/FRET emission ratio focusing on CIC structures. As shown in Fig. 1, G–I (entotic 1), while appearing inside another cell, inner cells exhibited an increase in IETD substrate cleavage and a drop in TMRM intensity similar to apoptotic cells. Later on, these cells showed a reduction in Venus fluorescence and accumulation of TMRM, indicating that they underwent entotic cell death (Fig. 1, G and H; entotic 1 and 2). In some cases, cells showing IETD substrate cleavage entered into neighboring cells but were released hours after internalization (Fig. 1, G–I; entotic 3). We also monitored spontaneous entotic events in control cells that were not exposed to TRAIL. Inner cells did not display any change in IETD substrate cleavage before entering or while inside outer cells during spontaneous entosis. However, reduction in Venus fluorescence intensity and TMRM fluorescence accumulation were still evident at later entotic stages (Fig. 1, E and F). These findings suggest that IETD substrate cleavage in inner cells during entosis was specifically related to TRAIL stimulation.

We next focused on whether IETD substrate cleavage changed in outer cells upon TRAIL stimulation. Remarkably, outer cells showed a slow IETD substrate cleavage similar to surviving cells in TRAIL treatment (Fig. 1 I; entotic 1, 2, and 3). To examine whether outer cells showed less substrate cleavage compared with neighboring apoptotic cells, we compared the maximum value of CFP/FRET emission ratio kinetics in outer cells in controls as well as in TRAIL-treated cells. We found that maximum IETD substrate cleavage values were significantly lower in outer cells compared with neighboring apoptotic cells. We observed no difference in CFP/FRET emission ratio when we compared outer cells with neighboring cells in untreated cultures (Fig. 1 J). To further confirm whether outer cells showed less caspase activation, we performed immunofluorescence staining and confocal microscopy analysis for cleaved caspase-3 in conjunction with nuclear staining in cells treated with or without TRAIL. As expected, TRAIL treatment resulted in a significant increase in cleaved caspase-3 intensity in all treated

cells compared with control cells (data not shown). In parallel, we observed that most inner cells ($83.57 \pm 5.78\%$) showed an increase in cleaved caspase-3 staining (Fig. S1 E). Moreover, we could occasionally observe fragmented nuclear morphology as well as the release of cytochrome *c* (data not shown) in a fraction of inner cells, indicating that these cells indeed showed to some degree “apoptotic features” during entosis. However, these markers were not detectable after lysosomal accumulation in inner cells during entotic cell death. In parallel with time-lapse experiments, we found that outer cells showed significantly lower levels of cleaved caspase-3 staining compared with neighboring apoptotic cells (Fig. 1 K). To examine long-term survival of outer cells, we monitored 42 entotic structures by time-lapse microscopy in HCT116 cells treated with TRAIL for 48 h. Based on cell morphology, TMRM, and Venus signal in outer cells, we found that 38 of 42 outer cells survived in TRAIL treatment. These findings suggest that cells that exhibit limited caspase activity might become outer cells during entosis, and this mechanism may provide a survival advantage during TRAIL-induced apoptosis.

Large-scale high-content screening platform-based quantification of simultaneous induction of entosis and apoptosis

Although entosis has a unique cytological structure, making the events possible to identify, we realized that there was a need to develop a large-scale unbiased method for entosis quantification. To address this, we sought to design an automated, large-scale analysis for simultaneous detection of entosis and cell death events by using a high-content screening (HCS) platform (Fig. 2). Briefly, cells that have been seeded into 96-well plates were labeled with Hoechst, propidium iodide (PI), and LysoTracker and exposed to different treatments (Fig. 2 A). After recording 36 random fields of view per treatment per experiment for 72 h, images were segmented using CellProfiler v2.2 and combined to analyze entotic events (Fig. 2, B and C). We were able to successfully detect entotic events based on Hoechst-stained

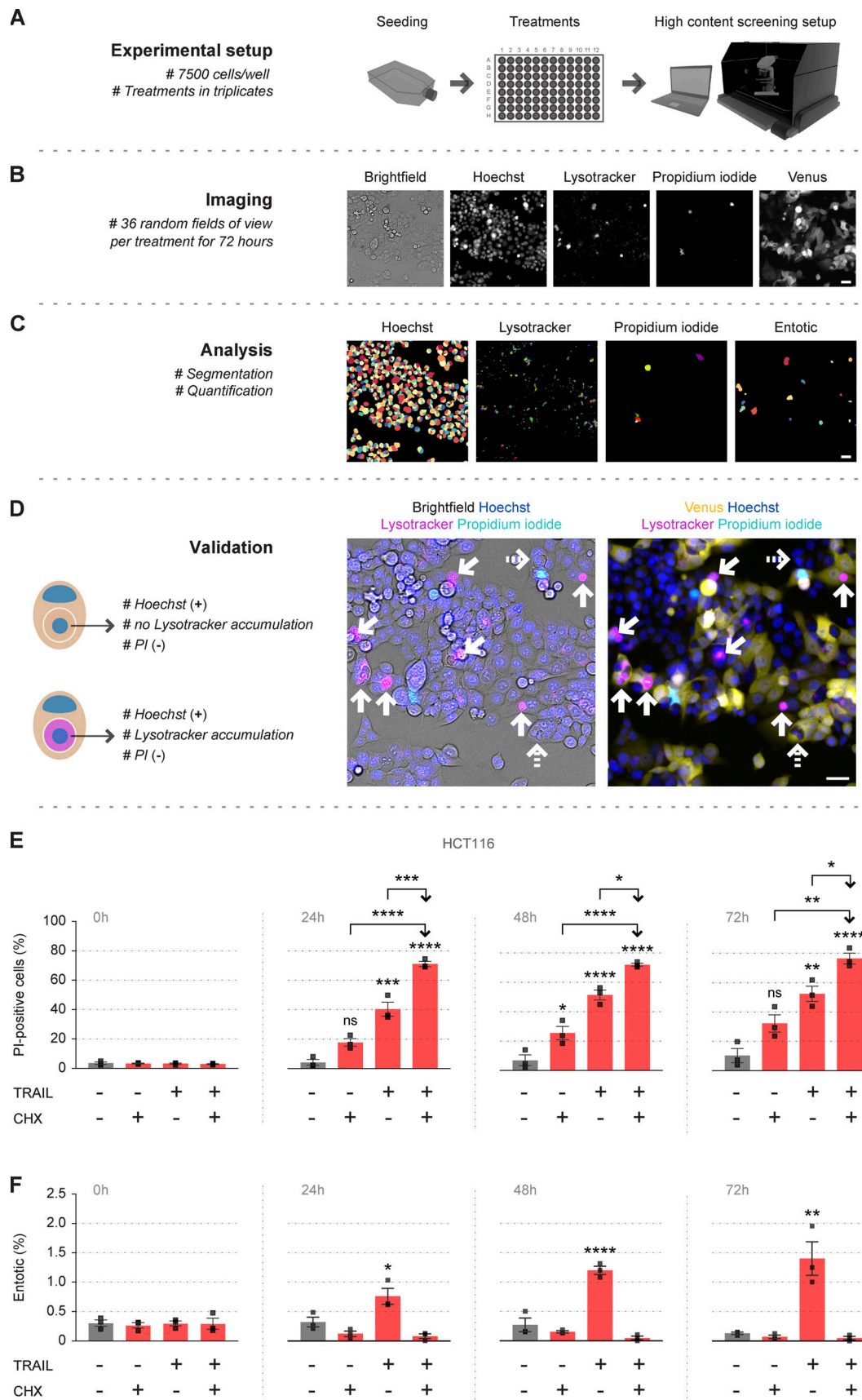


Figure 2. Large-scale HCS-based quantification of simultaneous induction of entosis and apoptosis upon TRAIL and TRAIL + CHX stimulation. (A–D) Overview of steps involved in HCS-based analysis of entotic structures. After seeding (7,500 cells/well), staining (Hoechst, LysoTracker, PI) and treatments

(A), 36 random fields of view per treatment per experiment were recorded for 72 h (B). CellProfiler defined cell nuclei, lysosomes, and PI-positive cells, then overlaid images were used to detect entosis events (C). Entosis events detected by CellProfiler were manually verified using overlaid images of brightfield, Hoechst (blue), LysoTracker (magenta), PI (cyan), and Venus (yellow) by analyzing Hoechst-stained and PI-negative inner cells within another Hoechst-stained and PI-negative cell showing a crescent-shaped nuclear morphology (D). Both inner cells that do (arrows) and do not (dashed arrows) show LysoTracker accumulation were quantified as entotic. Scale bars: 25 μm . **(E and F)** TRAIL, but not TRAIL + CHX, promotes entosis in HCT116 cells. Quantification of PI-positive cells (E) and entotic structures (F) in HCT116 cells treated with or without CHX, TRAIL, and TRAIL + CHX for 72 h. Data are shown as individual values for each experiment as well as mean \pm SEM ($n = 3$). Asterisks on top of individual bars indicate comparisons with control. *, $P < 0.05$; **, $P < 0.01$; ***, $P < 0.001$; **** $P < 0.0001$, by one-way ANOVA followed by Tukey's multiple comparison test.

and PI-negative inner cells within another Hoechst-stained and PI-negative cell showing a crescent-shaped nuclear morphology. Both inner cells that show and do not show LysoTracker accumulation were quantified as entotic (Fig. 2 D). Cells that showed PI uptake were considered dead. As expected, TRAIL significantly increased the number of PI-positive cells compared with control. Moreover, the presence of CHX further enhanced TRAIL-induced cell death (Fig. 2 E). In parallel with time-lapse imaging experiments, TRAIL resulted in a significant increase in entosis events in a time-dependent manner compared with control cells. In contrast, we observed a reduction in entosis events in the presence of CHX (Fig. 2 F). We obtained comparable results by manual entosis quantification in HCT116 as well as in other cell lines (breast, MCF-7; colon, LS180; Fig. S2, A and B). Moreover, spheroids prepared from HCT116 cells likewise showed a significant increase in entosis events in response to TRAIL treatment (Fig. S2 C and Video 5).

Characterization of entotic ultrastructures and features of entotic cell death induced by TRAIL treatment

Next, we performed a set of experiments for in-depth characterization of entosis events in controls and TRAIL-treated cells. First, we analyzed the morphological changes in early- and late-stage entotic structures by staining the plasma membrane (β -catenin), nuclei (Hoechst), and lysosomal accumulation (LysoTracker). As shown in Fig. 3, A and B, confocal imaging of early- and late-stage entosis events verified that inner cells were fully internalized. In line with previous findings (Overholtzer et al., 2007; Garanina et al., 2017), while β -catenin staining was detectable around inner cells at early stages, we did not detect β -catenin staining in inner cells at late stages, suggesting that β -catenin underwent degradation in inner cells during entotic cell death. We did not observe morphological differences in plasma membranes, nuclei, and lysosomal accumulation when we compared entotic structures in controls with the ones in TRAIL-treated cells. Thus, we focused on TRAIL-treated cells in further analysis.

To examine the cellular ultrastructures during TRAIL-induced entosis in detail, we performed correlative light and electron microscopy (CLEM) analysis in TRAIL-treated cells. First, we used 3D confocal microscopy to image Hoechst and LysoTracker staining in various stages of entosis. After verifying that inner cells were fully internalized, we performed transmission electron microscopy (TEM) analysis to observe the ultrastructures in the corresponding entosis events. As expected, at all stages, inner cells showed a round-shaped morphology within outer cells; an entotic vacuole between inner and outer cells was visible; and the nucleus of outer cells was pushed toward the periphery, forming a crescent-like shape (Fig. 3, C-E).

During the early stages, both inner and outer cells retained cell membranes; preserved cytoplasmic organelles; and exhibited an intact nuclear membrane, nucleoli, and dispersed chromatin (Fig. 3 C). During middle stages, we observed an increase in lysosomal staining as well as accumulation of several lysosomes, autophagosomes, and autophagolysosomes in inner cells (Fig. 3 D). We were able to further confirm autophagosome structures in the corresponding inner cell by immunogold labeling for LC3 (Fig. S3 A). Moreover, some mitochondria juxtaposed to lysosomes, autophagosomes, and/or autophagolysosomes but were not localized inside of them. Interestingly, when we looked at the nucleus of inner cells, we observed that some lysosomes and autophagosomes were localized in the areas where the nuclear membrane was disrupted (Fig. 3 D). During late stages, inner cells showed an increase in lysosomal staining colocalizing with nuclear staining. Furthermore, TEM analysis showed that both cytoplasmic and nuclear content of inner cells exhibited a complete degradation pattern. We could observe the remnants of inner cells; however, none of the cytoplasmic organelles were detectable (Fig. 3 F).

To fully explore the stages of entotic cell death during TRAIL treatment, we performed time-lapse microscopy in HCT116 cells transfected with lysosomal-associated membrane protein 1 (LAMP1)-mScarlet-I, an indicator of entotic cell death (Overholtzer et al., 2007). Because we used LysoTracker staining to detect late-stage entotic structures throughout our study, we also incubated the cells with LysoTracker to confirm colocalization of LAMP1 and lysosomal staining. As shown in Fig. 3 F, during internalization, lysosomes in both inner and outer cells showed a synchronous movement for a short time followed by simultaneous accumulation of both LAMP1 and LysoTracker staining at the membrane localized around the inner cell. As entotic cell death progressed, LAMP1 and LysoTracker staining increased inside the cytoplasm of the inner cell and eventually colocalized with nuclear staining. As expected, quantification of LAMP1 and LysoTracker intensities verified a complete colocalization at all stages (Fig. S3 B and Video 6). To examine whether late-stage inner cells underwent lysosomal cell death in TRAIL treatment, we performed 3D confocal microscopy analysis to measure cleavage of a specific fluorogenic cathepsin B substrate (Z-Arg-Arg-AMC) in TRAIL-treated cells. All inner cells that showed LysoTracker accumulation also showed a significant increase in cathepsin B activity (Fig. 3 G and Fig. S3 C), suggesting that late-stage entotic cells underwent cathepsin-B-mediated lysosomal cell death in TRAIL treatment.

Entosis induced by TRAIL requires DR4 and DR5 and structural presence of caspase-8

To investigate whether entosis or apoptosis inhibition affected each another, we performed large-scale HCS-based analysis and

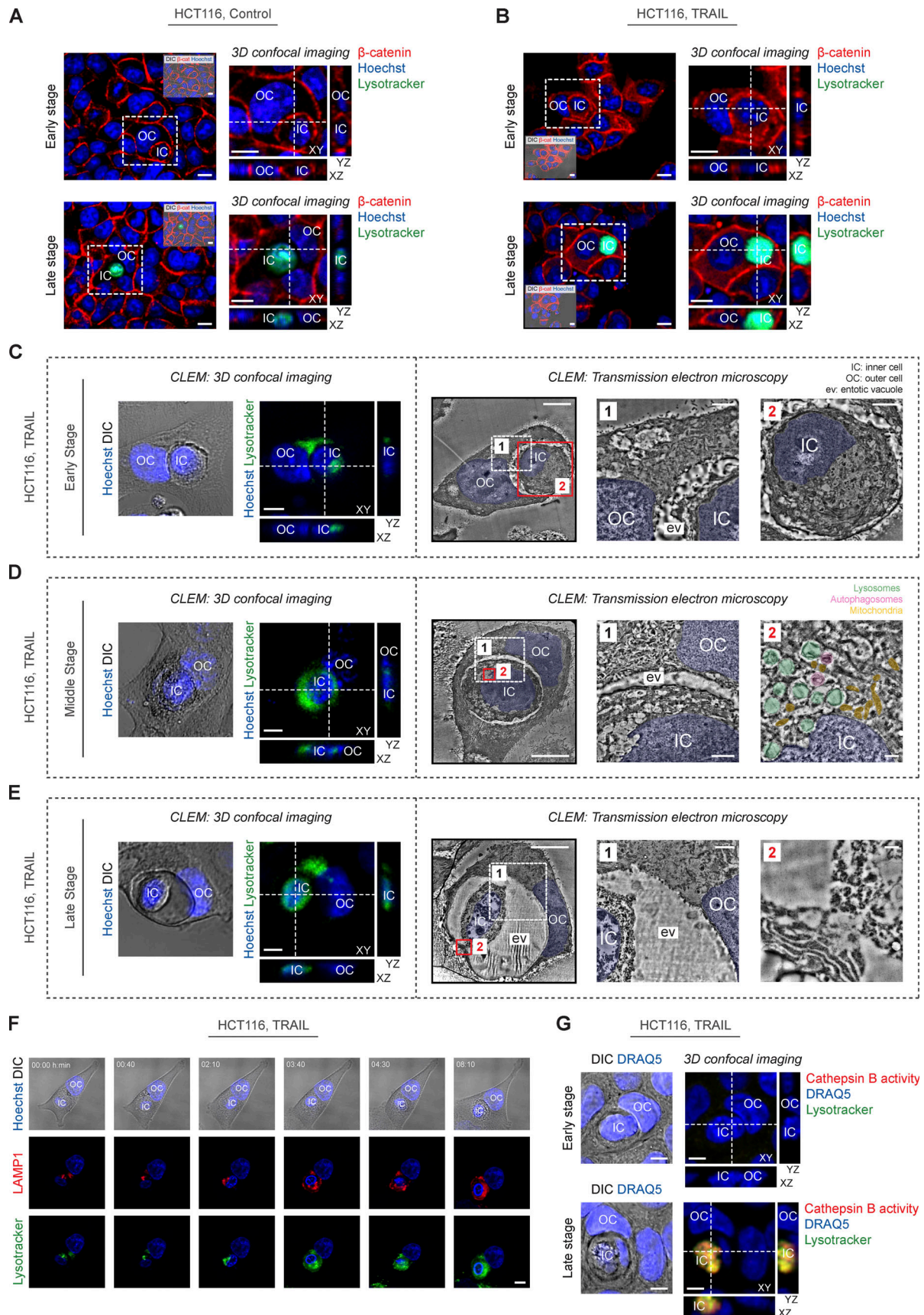


Figure 3. **3D confocal microscopy and CLEM analysis of structural features of entosis in TRAIL-stimulated HCT116 cells.** (A and B) 3D confocal microscopy imaging of β -catenin (red), Hoechst (blue), and LysoTracker (green) confirms complete cell internalization in control (A) and TRAIL-treated (B) cells.

Representative confocal images of early-stage (top) and late-stage (bottom) entotic structures are shown. Orthogonal views through z-stacks of depicted areas are shown next to each image. Scale bars: 10 μ m. **(C–E)** CLEM analysis of entotic ultrastructures in TRAIL-treated cells. Representative 3D confocal microscopy images of Hoechst (blue) and LysoTracker (green) staining of early (C), middle (D), and late (E) stages of entosis events are shown (left). Scale bar: 10 μ m. TEM images of corresponding entosis events are shown (right). Two depicted areas (white and red squares) imaged in higher magnifications are shown. Green, magenta, and yellow pseudocolored areas indicate lysosomes, autophagosomes, and mitochondria, respectively. Blue pseudocolored areas indicate nuclei. Scale bars in TEM images from left to right: 10 μ m, 2 μ m, and 1 μ m (C2) or 500 nm (D2 and E2). **(F and G)** Late-stage inner cells undergo cathepsin B-mediated lysosomal cell death. **(F)** Representative time-lapse images of LysoTracker staining (green) in HCT116 cells stably expressing Lamp1-mScarlet plasmid (red) showing an inner cell undergoing entotic cell death. Scale bar: 10 μ m. **(G)** Representative 3D confocal microscopy images of fluorogenic cathepsin B substrate (red), DRAQ5 (blue), and LysoTracker (green) of early- and late-stage entotic cells are shown. Scale bars: 10 μ m.

quantified the rate of apoptosis and entosis in the cells treated with or without TRAIL in the presence or absence of Y-27632 (ROCK 1/2 inhibitor), z-VAD-fmk (pan-caspase inhibitor), or z-IETD-fmk (caspase-8 inhibitor). We found that Y-27632, alone or in combination with TRAIL, did not affect the rate of PI-positive cells (Fig. 4 A) or cells with cleaved IETD substrate (Fig. S4 A), indicating that inhibition of ROCK signaling did not affect the induction of TRAIL-induced apoptosis. As expected, TRAIL treatment resulted in a significant increase in both PI-positive cells and cells with cleaved IETD substrate. Also, the presence of either z-VAD-fmk or z-IETD-fmk blocked TRAIL-induced increases in both PI-positive cells and cells with cleaved IETD substrate, confirming that cell death was due to induction of apoptosis (Fig. 4 A and Fig. S4 A). Interestingly, as shown in Fig. 4, B and C, and Fig. S5 B, quantification of entotic structures showed that the presence of either z-VAD-fmk or z-IETD-fmk did not affect the rate of entosis in control or TRAIL-treated cells, suggesting that inhibition of caspase activity did not affect the rate of entosis. As expected, the presence of Y-27632 inhibited the rate of entosis induced by TRAIL treatment as well as in controls. Taken together, these findings suggest that the internalization process during entosis is not dependent on caspase activity.

To examine whether TRAIL death receptors DR4 and DR5 were involved in induction of entosis by TRAIL, we quantified PI-positive cells and entotic structures in *DR4^{-/-} DR5^{-/-}* cells (Dufour et al., 2017). As expected, TRAIL treatment did not change the rate of PI-positive cells in *DR4^{-/-} DR5^{-/-}* cells compared with controls (Fig. 4 D). Deficiency in DR4 and DR5 was confirmed by Western blot (Fig. 4 E). Strikingly, there was no difference in entosis rate between control and TRAIL-treated *DR4^{-/-} DR5^{-/-}* cells, suggesting that death receptors were required for TRAIL-induced entosis (Fig. 4 F). To further evaluate whether death receptors were required for inner or outer cells, we labeled WT cells with CellTracker Green, labeled *DR4^{-/-} DR5^{-/-}* cells with CellTracker Red, and treated the cocultured cells with or without TRAIL in the absence or presence of z-VAD-fmk or Y-27632. We then imaged the cells by HCS and quantified the frequency of inner and outer cells. As expected, the presence of Y-27632 blocked entosis formation in all treatment groups (data not shown). Remarkably, we found that inner cells were mostly WT cells regardless of treatment, whereas *DR4^{-/-} DR5^{-/-}* cells were dominantly outer cells, suggesting that death receptors may be required for inner cells during cell internalization (Fig. 4, G and H).

Caspase-8 sits at the nexus of death and survival pathways downstream of TRAIL signaling. In the past few years, a

nonapoptotic (nonenzymatic) role of caspase-8 has emerged in switching TRAIL signaling to survival pathway activation in cancer cells (Henry and Martin, 2017; Hartwig et al., 2017). To examine whether caspase-8 played a nonenzymatic role in the induction of entosis in TRAIL-treated cells, we first quantified PI-positive cells and entotic structures in *CASP8^{-/-}* cells (Henry and Martin, 2017). As expected, TRAIL treatment did not change the rate of PI-positive cells in *CASP8^{-/-}* cells compared with controls (Fig. 4 I). Deficiency in caspase-8 was confirmed by Western blot (Fig. 4 J). Remarkably, we observed no difference in the rate of entosis between control and TRAIL-treated *CASP8^{-/-}* cells, suggesting that caspase-8 may be required for TRAIL-induced entosis (Fig. 4 K). To further assess the nonenzymatic role of caspase-8, we reintroduced an expression plasmid for catalytically inactive *CASP8* mutant (C360A) into *CASP8^{-/-}* cells (Fig. 4 J). We found that reinsertion of active site mutant *CASP8* restored TRAIL-induced entosis compared with empty vector-transfected controls, suggesting that caspase-8 indeed plays a nonenzymatic role during TRAIL-induced entosis (Fig. 4 K). Interestingly, we observed a trend of increase in entosis events in control-treated *CASP8^{-/-}* cells compared with control-treated WT cells over time, with the difference statistically significant at 72 h. As expected, the presence of Y-27632 significantly inhibited the rate of entosis in all treatment groups in *CASP8^{-/-}* and *CASP8* C360A mutant cells (Fig. 4 K). Of note, when we cultured *CASP8^{-/-}* cells in glucose-deprived conditions, a known inducer of entosis (Hamann et al., 2017), we could still observe a significant increase in the rate of entosis, indicating that involvement of caspase-8 in TRAIL-induced entosis can be uncoupled from “canonical” entosis signaling (Fig. S4 C).

Inhibition of apoptosis alters inner cell fate toward release

Studies have shown that inhibition of apoptosis either genetically by overexpressing BCL-2 (Florey et al., 2011) or pharmacologically by using caspase inhibitors (Martins et al., 2018) results in release of inner cells during entosis. To examine this in the context of TRAIL treatment, we performed inner cell fate analysis using time-lapse microscopy (Fig. 5) after inhibiting apoptosis pharmacologically by z-VAD-fmk or genetically by using *BAX^{-/-} BAK^{-/-}* cells (Fig. 5 B). We found that the majority of inner cells underwent entotic cell death in WT control cells, and TRAIL treatment did not affect the frequency of inner cell death. However, treatment with z-VAD-fmk, alone or in combination with TRAIL, resulted in a significant reduction in inner cell death and increased the frequency of inner cells that are released from their hosts. Strikingly, in *BAX^{-/-} BAK^{-/-}* cells, the majority of inner cells did not undergo entotic cell death;

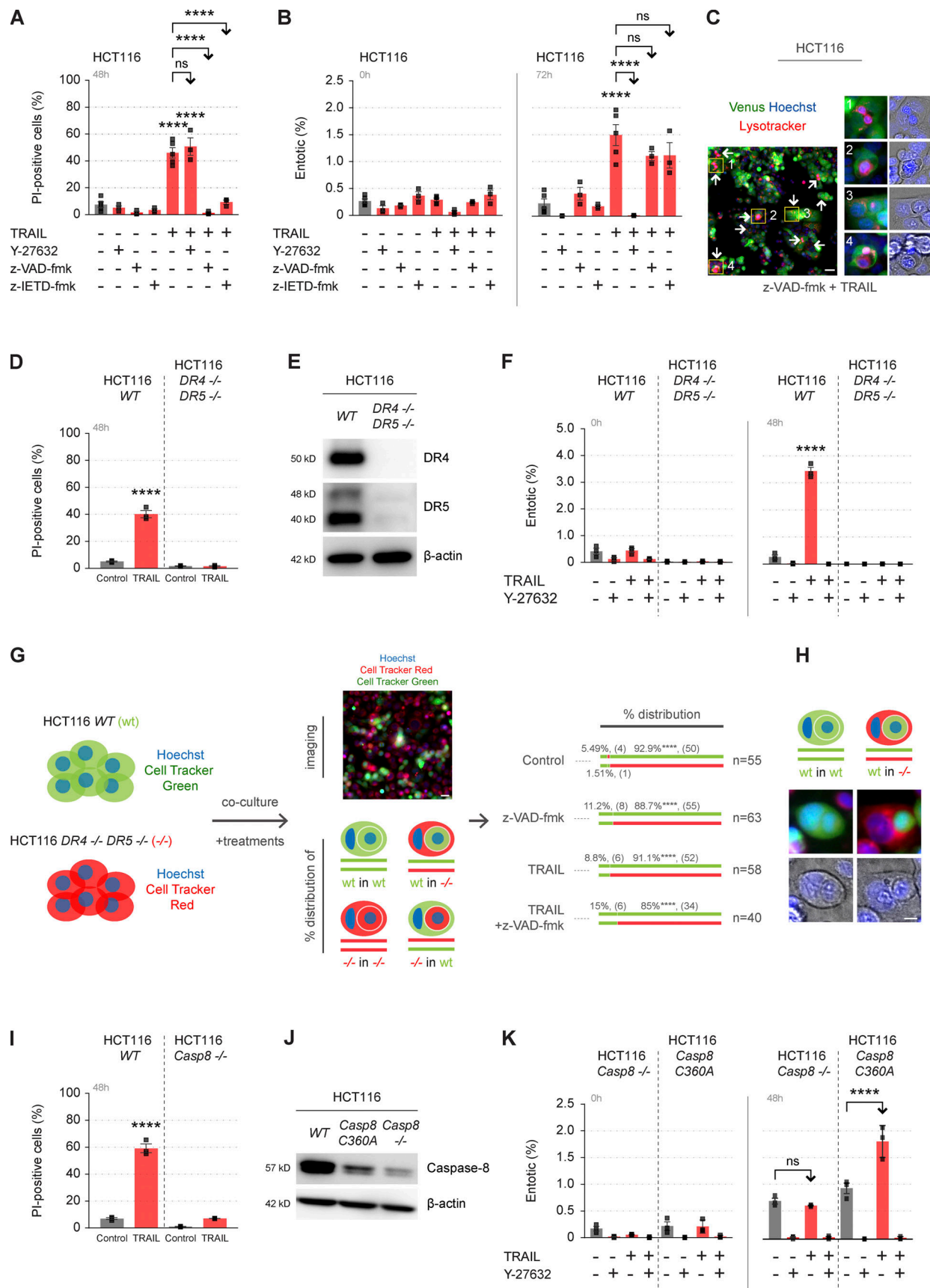


Figure 4. Entosis induced by TRAIL requires death receptors and structural presence of caspase-8. (A–C) Internalization process during entosis is independent of caspase activity. (A) Inhibition of entosis does not affect the rate of TRAIL-induced apoptosis. Quantification of PI-positive cells in HCT116 cells

treated with or without TRAIL in the absence or presence of z-VAD-fmk, z-IETD-fmk, or Y-27632. **(B and C)** Inhibition of caspase activity does not affect the rate of TRAIL-induced entosis. **(B)** Quantification of entotic structures in HCT116 cells treated with or without TRAIL in the absence or presence of z-VAD-fmk, z-IETD-fmk, or Y-27632. **(C)** Representative field of view from HCS-based entosis analysis is shown. Arrows indicate entotic events, four representative events are depicted and shown. Scale bar: 50 μ m. **(D–H)** TRAIL death receptors are required for cell internalization during TRAIL-induced entosis. **(D)** Quantification of PI-positive cells in HCT116 WT and *DR4^{-/-} DR5^{-/-}* cells treated with or without TRAIL. **(E)** Western blot images of DR4 and DR5 expressions in HCT116 WT and *DR4^{-/-} DR5^{-/-}* cells. β -Actin was used as loading control. **(F)** Quantification of entotic structures in HCT116 WT and *DR4^{-/-} DR5^{-/-}* cells treated with or without TRAIL in the absence or presence of Y-27632. **(G and H)** DR4 and DR5 are required for inner cells during cell internalization. **(G)** HCT116 WT and *DR4^{-/-} DR5^{-/-}* cells were labeled with CellTracker Green and CellTracker Red, mixed in 1:1 ratio, and treated with or without TRAIL in the absence or presence of z-VAD-fmk. Images were recorded by HCS and analyzed using CellProfiler. Scale bar: 25 μ m. Distribution of entosis events divided into four subcategories as indicated; absolute numbers are shown in parenthesis. Data are shown as mean from three experiments. *n* indicates number of events analyzed per group. **(H)** Representative images showing entotic structures formed between “wt in wt” (green) and “wt in $-/-$ ” (green and red, respectively) cells. Scale bar: 10 μ m. **(I–K)** Induction of entosis by TRAIL requires structural presence of caspase-8. **(I)** Quantification of PI-positive cells in HCT116 WT and *Casp8^{-/-}* cells treated with or without TRAIL. Data are shown as mean \pm SEM from three experiments. **(J)** Western blot images of *CASP8* expression in HCT116 WT, *CASP8* C360A mutant, and *CASP8^{-/-}* cells. β -Actin was used as loading control. **(K)** Quantification of entotic structures in *CASP8^{-/-}* and *CASP8* C360A mutant cells treated with or without TRAIL in the absence or presence of Y-27632. Data are shown as individual values for each experiment as well as mean \pm SEM from three experiments except as noted in G and I. ****, $P < 0.0001$ by one-way ANOVA followed by Tukey’s multiple comparison test (A, B, D, F, G, I, and K).

instead, they were released regardless of treatment (Video 7). There was no difference in inner cell division among treatments in WT and *BAX^{-/-} BAK^{-/-}* cells (Fig. 5 C). As expected, *BAX^{-/-} BAK^{-/-}* cells were resistant to TRAIL-induced apoptosis, and pretreatment with Y-27632 blocked the formation of entotic structures in controls as well as TRAIL-treated WT and *BAX^{-/-} BAK^{-/-}* cells (data not shown). To further examine whether *BAX* and *BAK* are involved in regulating downstream entotic cell death, we examined cathepsin B activity and LysoTracker accumulation in late-stage entotic cells by 3D confocal microscopy. As shown in Fig. 5 D, inner cells exhibited LysoTracker accumulation colocalizing with increased cathepsin B activity in all treatments, confirming that inner cells were undergoing entotic cell death during analysis. We observed no morphological difference in late-stage entotic cells among treatments in either WT or *BAX^{-/-} BAK^{-/-}* cells (Fig. 5 D). Likewise, quantification of the mean fluorescence intensity of cathepsin B substrate cleavage in inner cells yielded no significant change among treatments and cell lines (Fig. 5 E). Collectively, our findings suggest that inhibition of apoptosis signaling changes inner cell fate toward release. Moreover, the decision of inner cell fate does not occur during late stages of entotic cell death but might rather be made during earlier stages of entosis.

Clinical association among TRAIL signaling, CIC structures, and CRC

We investigated the relationship among CIC structures, expression of proteins involved in TRAIL signaling, clinicopathological characteristics, and outcome in a cohort of stage 2 and 3 CRC patients from the NI240 phase III clinical trial randomly assigned to either observation or chemotherapy (5-fluorouracil [5-FU]/leucovorin) after resection (McLornan et al., 2010). Demographic and clinicopathological characteristics of the CRC patient cohort are summarized in Table S1 and Fig. S5 A. We blindly quantified CIC structures in high-quality hematoxylin and eosin (H&E)-stained tissue microarray (TMA) cores from 232 distinct patients prepared from the center of the tumor ($n = 648$), invasive front of the tumor ($n = 210$), and adjacent normal tissue ($n = 552$). Besides H&E staining, a combination of different cytoplasmic and nuclear staining has been used to detect CIC structures (Mackay et al., 2018). Therefore, we increased the

sample size up to six consecutive TMA sections by quantifying CIC structures in the TMA cores ($n = 1,381$) of tyrosine-protein kinase Met (c-MET; stains both the cytoplasm and the cell membrane) and nuclear staining (hematoxylin) prepared from the same tissues (center of the tumor, $n = 636$; invasive front of the tumor, $n = 210$; matched normal, $n = 535$; Fig. 6 A). We observed a strong correlation when comparing CIC events identified from H&E-stained and c-MET-stained TMA cores (Fig. S5 B). Thus, for downstream analyses, we pooled CIC structures estimated from either staining and considered them as biological replicates, totaling up to two and six cores per patient for tissue from the invasive front and tumor center/matched normal tissue, respectively. Notably, the distribution of CIC structures in tumors showed a high heterogeneity among different sections within the same patient as well as across patients (Fig. 6 B). We then focused on patients with CIC quantifications from tumor center, invasive front, and matched normal tissues. We found that the number of CIC events differed by location, decreasing from the tumor center to the invasive front and further into the matched normal tissue (Fig. 6, C and D). We further explored the relationship between CIC structures by tissue and clinicopathological features. We found no statistically significant difference in between CIC structures and tumor size, spread, and metastasis (TNM) staging, age, sex, lymphovascular invasion, and treatment. However, we observed fewer CIC structures in rectal tumors compared with those from the colon ($P = 0.009$; Table S2 and Fig. S5 C).

Next, we examined the association between CIC structures and proteins involved in the TRAIL signaling pathway, including TRAIL, TRAIL/R1 (DR4), TRAIL/R2 (DR5), c-FLIP, and caspase-8, in tumor tissue. In agreement with other reports (Mackay et al., 2018; Schenker et al., 2017), a proportion of patients (75 of 211, 36%) showed no evidence of CIC structures in tumor tissues. Thus, we used the absence or presence of CIC structures as the cutoff and classified the CRC patients in our cohort as CIC absent (CIC = 0) or CIC present (CIC >0) if the median number of CIC structures detected across multiple biological replicas within the same tissue was ≥ 0 , respectively. Remarkably, we found that CIC-positive tumors had a higher expression of TRAIL and c-FLIP, with a trend toward higher expression of *CASP8* (Fig. 6 E).

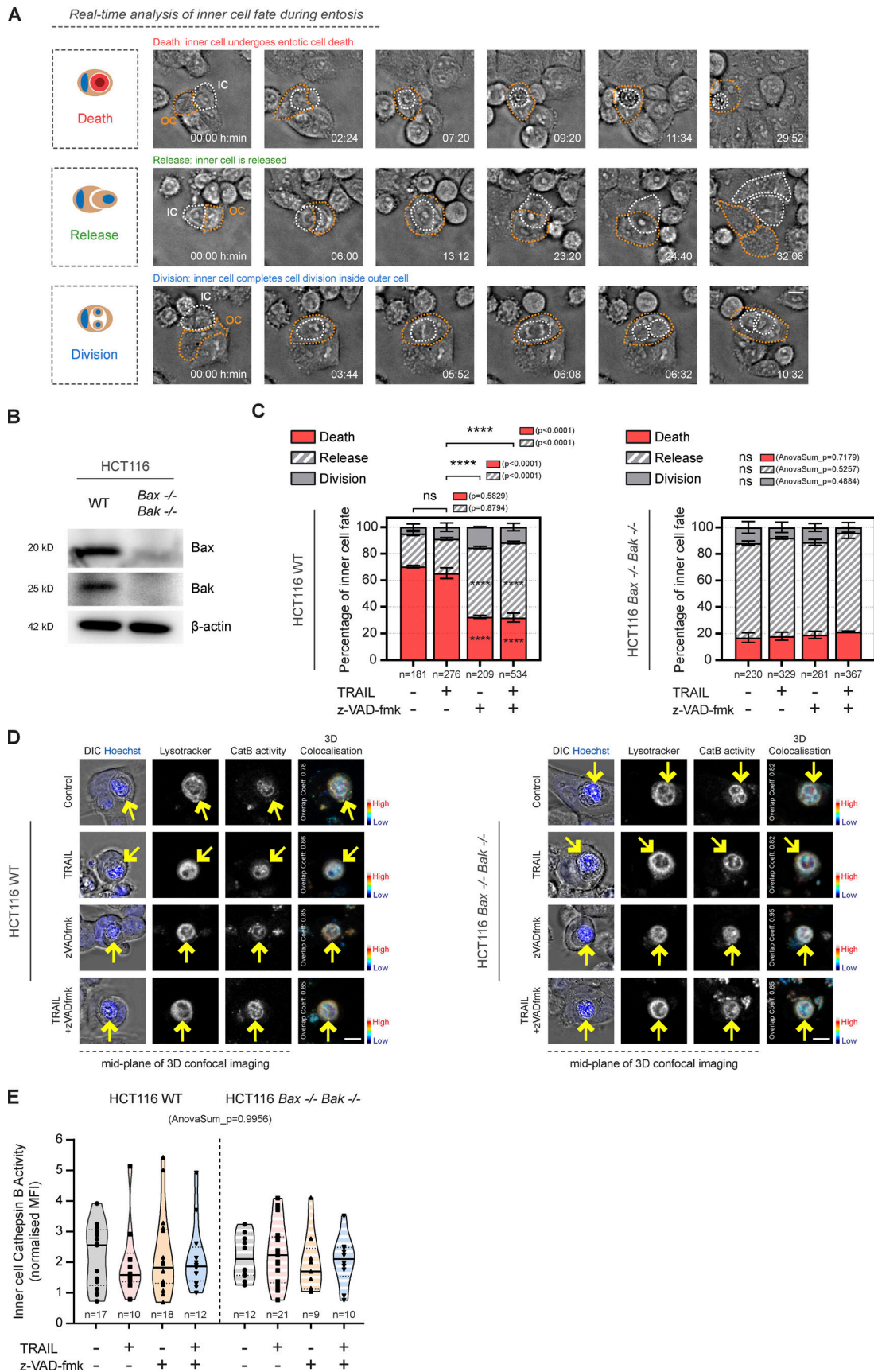


Figure 5. Deletion of *Bax* and *Bak* or inhibition of caspase activation alters inner cell fate toward release. (A) Schematic representation of inner cell fates and representative time-lapse images showing that the inner cell undergoes entotic cell death, the inner cell is released, and the inner cell completes cell

division. Inner and outer cells are indicated as orange and white dashed lines, respectively. Scale bar: 10 μm . **(B)** Western blot images of *Bax* and *Bak* expressions in HCT116 WT and *Bax*^{-/-} *Bak*^{-/-} cells. β -Actin was used as loading control. **(C)** Quantification of inner cell fates in HCT116 WT and *Bax*^{-/-} *Bak*^{-/-} cells treated with or without TRAIL in the absence or presence of z-VAD-fmk. Data are shown as individual values for each experiment as well as mean \pm SEM. *n* is the total number of cells analyzed over 48 h from three experiments. Asterisks inside individual bars indicate comparisons with control. *****, $P < 0.0001$ by one-way ANOVA followed by Tukey's multiple comparison test. **(D)** Representative 3D confocal microscopy images of DIC, Hoechst (blue), LysoTracker, and fluorogenic cathepsin B substrate of late-stage entotic cells in WT and *Bax*^{-/-} *Bak*^{-/-} cells treated with or without TRAIL in the presence or absence of z-VAD-fmk. 3D colocalization of LysoTracker and cathepsin B substrate is visualized. Yellow arrows indicate inner cells. Scale bars: 10 μm . **(E)** Quantification of cathepsin B activity in late-stage entotic inner cells in WT and *Bax*^{-/-} *Bak*^{-/-} cells treated with or without TRAIL in the presence or absence of z-VAD-fmk. Data are shown as individual values for each cell as well as median and quartiles. Statistical significance was tested using unpaired two-tailed *t* test. *n* is the total number of cells analyzed. CatB, cathepsin B; IC, inner cell; MFI, mean fluorescence intensity; OC, outer cell.

We next investigated the association between CIC structures and clinical outcome with Kaplan–Meier estimates and (un)adjusted Cox regression hazard models. There was no difference in disease-free survival (DFS) and disease-specific survival (DSS) curves when comparing patients with CIC structures (CIC >0) and those with no CIC structures (CIC = 0) detected in tumor center when examining the whole cohort or when stratifying by stage. Intriguingly however, patients with CIC structures (CIC >0) in the invasive front of the tumors had an approximately twofold increase risk of relapse (hazard ratio [HR], 1.64; $P = 0.051$) and cancer-related death (HR, 1.89; $P = 0.02$) compared with patients with no detected CIC structures (CIC = 0; Fig. 6 F). Moreover, the presence/absence of CIC structures in the invasive front of the tumor was an independent prognostic marker after controlling for baseline clinicopathological characteristics (DFS: HR, 2.01 [$P = 0.007$]; DSS: HR, 2.13 [$P = 0.006$]). We then assessed whether the association between CIC structures and clinical outcome differed by stage (2 versus 3). We found that the prognostic value of CIC structures in the invasive front region was seen only in stage 3 patients ($P = 0.02$ and $P = 0.04$ for DFS and DSS, respectively; Fig. 6, G and H). In a multivariate analysis controlling for baseline clinicopathological characteristics, among stage 3 patients, those who were CIC positive showed an increased risk of relapse (HR, 2.67; 95% confidence interval [CI], 1.31–5.43; $P = 0.004$) and cancer-related mortality (HR, 2.33; 95% CI, 1.12–4.87; $P = 0.02$). These associations were null among stage 2 patients. Taken together, these results suggest that the invasive front of tumors is the region where CIC structures have clinical relevance in stage 3 CRC patients.

Discussion

Recent studies have revealed that molecules that are known inducers of apoptosis in fact simultaneously activate multiple cell death and survival mechanisms in cancer cells, such as autophagy (Fitzwalter et al., 2018), necroptosis (Lin et al., 2016), and entosis (Durgan et al., 2017). In this study, we have discovered that CRC cells simultaneously initiate entosis and apoptosis upon TRAIL stimulation. The TRAIL signaling pathway is activated by immune effector cells, such as cytotoxic T cells and natural killer cells, and is also a promising therapeutic target for cancer treatment; however, frequently only a proportion of cancer cells undergo apoptosis despite exposure to saturating concentrations of TRAIL (Roux et al., 2015). Cell-to-cell variability, stochastic genetic fluctuations, and nongenetic differences among individual cells seem to be the main driving factors

resulting in the fractional killing. Here, measurement of single-cell caspase activation kinetics and MOMP upon TRAIL stimulation in HCT116 cells corroborated previous findings (Hellwig et al., 2008) that TRAIL treatment results in heterogeneous apoptosis activation. Strikingly, while analyzing the time of MOMP in single cells, we discovered that instead of showing a typical sharp decrease during apoptosis (Flusberg and Sorger, 2013), a small proportion of cells displayed a dramatic increase in TMRM signal. Although TMRM has been widely used in staining mitochondrial membrane potential in living cells (Hellwig et al., 2008), we could not find any study reporting a similar behavior of TMRM. This unanticipated behavior led us to track these cells in time-lapse images and revealed that TMRM accumulation occurred after a cell invaded into another cell, a process known as entosis. Costaining of TMRM and lysosomes demonstrated that TMRM accumulation was coincident with the acidification of inner cells during entotic cell death.

In this study, we improved some of the current limitations of entosis quantification by designing a large-scale HCS-based approach, which allows simultaneous detection of apoptosis and entosis continuously without requiring any processing step, such as washing or trypsinization. Our fully customizable approach randomly records several fields of view and enables quantification of a large number of cells over time. It automatically detects the late-stage entosis events, and most importantly, cells are monitored in their natural state in culture conditions throughout the experiment. Entosis was initially found to be induced by matrix detachment in human mammary epithelial cells and breast cancer cells (Overholtzer et al., 2007). Further studies have revealed that several factors can induce entosis such as myosin activation (Wan et al., 2012), epithelial cadherin expression (Hamann et al., 2017), glucose starvation (Hamann et al., 2017), radiation, and chemotherapeutics, such as paclitaxel, oxaliplatin, and cisplatin (Durgan et al., 2017), in attached cell lines. Our HCS-based quantification demonstrated that TRAIL stimulation promoted entosis in CRC cells in a time-dependent manner. We were able to confirm entosis induction by TRAIL also in different cell line models as well as spheroids. Intriguingly, the presence of CHX significantly increased TRAIL-induced apoptosis but reduced the rate of entosis. Given that CHX enhances TRAIL-induced apoptosis by reducing key survival proteins, such as MCL-1 and c-FLIP (Brooks and Sayers, 2005; Hellwig et al., 2008), induction of entosis by TRAIL might be related to prosurvival signaling. Pretreatment with the pan-caspase inhibitor z-VAD-fmk inhibited TRAIL-induced caspase activation and apoptosis; however, it did not affect the induction

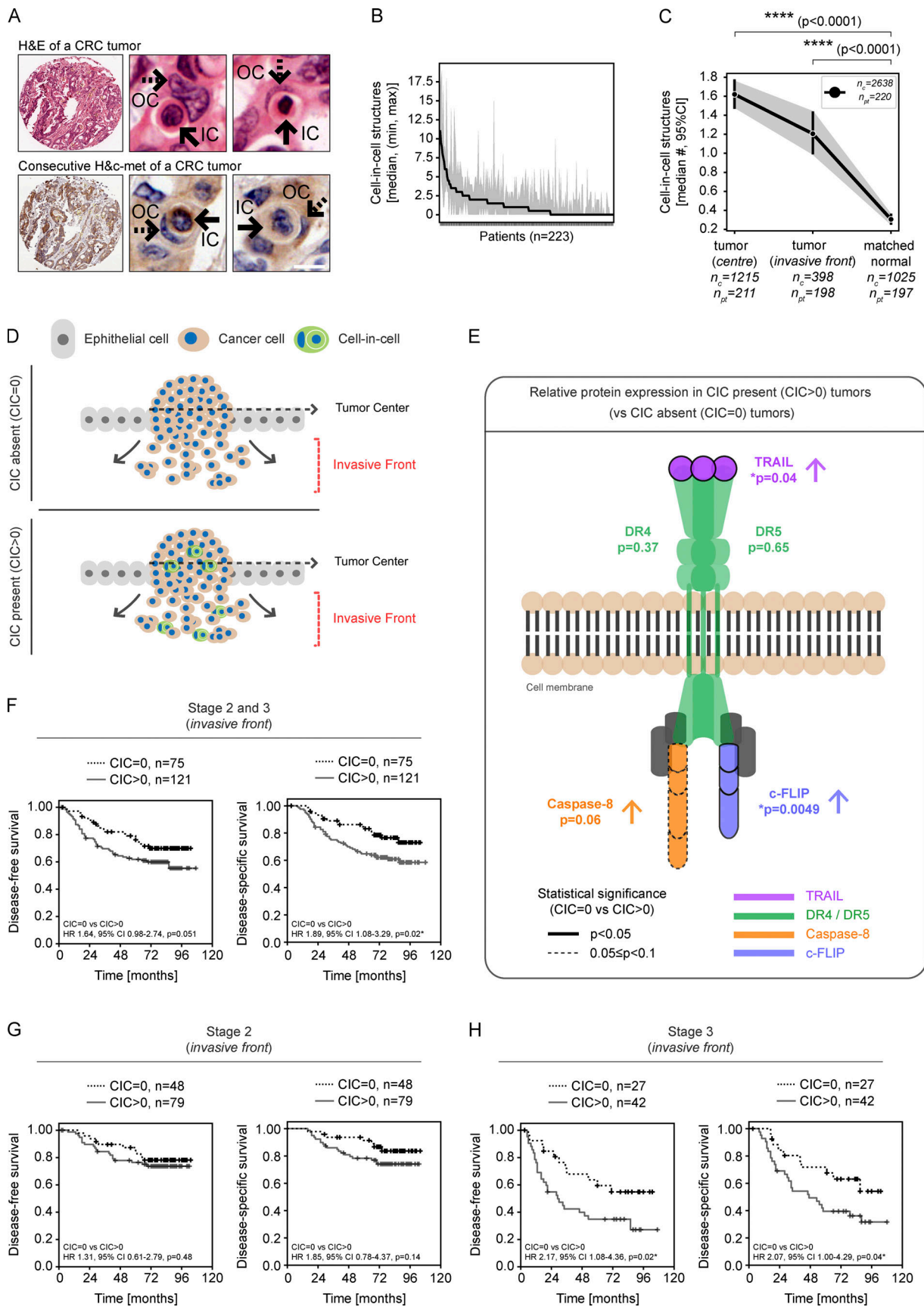


Figure 6. **Clinical association among TRAIL signaling, CIC structures, and CRC.** (A–C) CIC structures are increased in CRC tumors compared with matched normal tissues. (A) Consecutive H&E (top) and hematoxylin/c-Met (H&c-MET; bottom) sections showing representative CIC structures in a CRC tumor. Plain

arrows indicate inner cells, and dashed arrows indicate outer cells. Scale bar: 10 μ m. **(B)** Inter- and inpatient heterogeneity in CIC events detected in tumor tissue and computed for each patient of the NI240 cohort ($n = 223$). Patients (x-axis) are sorted in decreasing order of median CIC events (y-axis) detected in individual TMA cores prepared from tumor tissue and stained with either H&E or c-MET. Line and shaded area indicate the median and the minimum and maximum number of CIC structures across the cores for each patient, respectively. **(C)** Quantification of CIC structures in TMA sections prepared from tumor center, invasive front, and matched normal tissues. n_c and n_{pt} indicate number of tumor cores and patients, respectively. ****, $P < 0.0001$. **(D)** Schematic representation of the absence or presence of CIC structures and the center and the invasive front regions of a tumor. **(E)** Overexpression of proteins involved in TRAIL signaling is associated with presence of CIC structures in CRC tumors. Association among expression levels of TRAIL, DR4, DR5, caspase-8, c-FLIP, and CIC structures. Relative protein expression between CIC absent (median CIC = 0) and CIC present (median CIC >0) tumors is shown. Statistically significant differences in protein expression between CIC absent and CIC present patients are indicated by solid line ($P < 0.05$) and dashed line ($0.05 \leq P < 0.1$). Individual P values are shown under each protein. *, $P < 0.05$. **(F–H)** Presence of CICs in the invasive front region of tumors is an independent prognostic marker for DFS and DSS in CRC. Kaplan–Meier estimates of DFS and DSS of the NI240 cohort (F) comparing stage 2 (G) and stage 3 (H) CRC patients grouped by the presence or absence of CIC structures in the invasive front region. *, $P < 0.05$. IC, inner cell; OC, outer cell.

of entosis by TRAIL. On the contrary, pretreatment with the ROCK inhibitor Y-27632, which effectively blocks entosis without affecting phagocytosis-like activity (Tonnessen-Murray et al., 2019), inhibited TRAIL-induced entosis but did not affect caspase activation or induction of apoptosis by TRAIL. Thus, our results suggest that entosis and apoptosis are simultaneously induced by TRAIL; in addition, caspase activation during apoptosis is not involved in the cell internalization process during entosis.

During induction of apoptosis, binding of TRAIL to DR4 and DR5 leads to receptor trimerization and formation of death-inducing signaling complex, which further activates caspase-8 by homodimerization (Walczak, 2013). Here, we explored the role of upstream TRAIL signaling in the context of entosis induction. Our findings suggest that DR4 and DR5 are required for induction of entosis by TRAIL. Moreover, we show that cells that do not express DR4 and DR5 are likely to become outer cells when cocultured with their WT counterparts. On the other hand, cells expressing those receptors dominantly become inner cells, suggesting that TRAIL signaling acts on inner cells during cell internalization. In parallel with these findings, results from our time-lapse experiments suggest that cells that show limited caspase activation upon TRAIL stimulation become outer cells, whereas inner cells can display caspase activity similar to apoptotic cells. Because DR4 and DR5 share a high structural homology (~58%) and both can activate downstream signaling (Walczak, 2013), it would be worthwhile to investigate whether either or both of these receptors regulate cell internalization during entosis, especially in the context of TRAIL-receptor endocytosis (Reis et al., 2017). Recent studies have revealed that caspase-8 plays a nonenzymatic role in activating prosurvival TRAIL signaling, leading to induction of nuclear factor- κ B-dependent cell survival and release of several cytokines that create a tumor-supportive microenvironment and promote tumor growth (Hartwig et al., 2017). We showed that pretreatment of z-IETD-fmk, a selective caspase-8 inhibitor, inhibited TRAIL-induced caspase activation and apoptosis but did not affect the rate of entosis induced by TRAIL. Remarkably, deletion of *CASP8* resulted in a reduction in TRAIL-induced entosis as well as apoptosis. Moreover, we were able to demonstrate that the induction of entosis was due to a nonenzymatic role of *CASP8*, as reinsertion of active site mutant *CASP8* (C360A) restored TRAIL-induced entosis. Taken together, our findings provide a new perspective to induction of entosis and

yet reveal another biological example for a nonenzymatic role of caspase-8.

While apoptotic cells show caspase activation and DNA fragmentation, entotic cell death involves recruitment of autophagic lipidation machinery proteins, including LC3, ATG5, ATG7, and VPS34, onto entotic vacuole, followed by recruitment of LAMP1, leading to lysosomal fusion ultimately resulting in inner cell death by cathepsin B release (Florey et al., 2011). However, in our study, inner cells occasionally showed features of apoptosis signaling during TRAIL treatment, such as caspase activation, cytochrome c release, and membrane blebbing. Strikingly, when entotic cell death started taking place, apoptotic features were not detectable after a certain stage, possibly due to acidification of inner cells. Florey et al. (2011) showed that inner cells can upregulate autophagy to survive within outer cells, and it has been well documented that inner cells can divide inside outer cells or can be released (Krishna and Overholtzer, 2016). Although activation of apoptosis does not seem to be involved in the induction of entosis in many systems, accumulating evidence suggests that blocking apoptosis either pharmacologically by caspase inhibitors (Martins et al., 2018) or genetically by overexpressing antiapoptotic genes, such as BCL-2 (Florey et al., 2011), results in the release of inner cells. Similarly, in this study, inner cell fate analysis showed that the majority of inner cells underwent entotic cell death unless cotreatment with z-VAD-fmk or knockout of BAX and BAK altered inner cell fate toward survival and release. Our experiments suggest that even though lysosomal cell death will eventually degrade a proportion of inner cells during TRAIL-induced entosis, the presence of BAX and BAK, as well as caspase activity, may still be necessary for entotic cell death to occur.

CIC structures have been reported in a variety of human cancers for more than a century (Overholtzer and Brugge, 2008); however, understanding their clinical relevance has progressed very little because studies have been mostly occasional reports limited to showing examples in the tumor tissues. Until now, to the best of our knowledge, there is no study assessing whether tumors have an increase in CIC structures compared with normal tissues in the same patients. Here, in addition to addressing this question, we performed a comprehensive clinical analysis of CIC structures in CRC patient samples. In line with the literature (Schenker et al., 2017), the number of CIC structures greatly varied among consecutive TMA sections from the same patient as well as among patients,

suggesting that multiple sections should be used to get a robust quantification of CIC structures in clinical samples. Intriguingly, CRC tumors showed significantly more CIC structures compared with matched normal tissues. Notably, CIC structures were not associated with clinicopathological features of CRC, including TNM staging, age, sex, lymphovascular invasion, and treatment. Remarkably, overexpression of TRAIL and c-FLIP but not DR4 and DR5 were associated with the presence of CIC in CRC tumors. These tumors also showed a trend to express higher levels of caspase-8. Taken together, in addition to our *in vitro* findings, our results suggest that TRAIL signaling is also clinically associated with the presence of CIC structures in CRC patients.

CICs have been reported not only in the center of tumors but also in the invasive front region in cancers (Schenker et al., 2017). However, whether the presence of CIC structures in different intratumoral regions has prognostic value was unknown. We show that the prognostic value of CIC structures emerges from their presence in the invasive front region of tumors but not in the tumor center in CRC. The invasive front region consists of the most progressed tumor cells, which invade into immune cell-rich stroma (Zlobec and Lugli, 2009). Due to higher immune cell content, this region may possess higher cytokine (and death ligand) content and might reflect greater interactions between immune cells and cancer cells (Sag et al., 2019). CRC cells have been shown to escape from natural killer cell-mediated tumor surveillance by acquiring resistance to TRAIL-mediated apoptosis *in vitro* (HCT116) and *in vivo* (Moriwaki et al., 2009). The *in vitro* as well as clinical data presented in this study might be a motivation for further investigations to evaluate whether CIC structures play a role in this immune cell-tumor cell interaction in the invasive front region. The invasive front is especially important in CRC as tumor budding, an established prognostic factor for CRC patients, occurs in this region (Koelzer et al., 2016). Because tumor buds consist of isolated tumor cells or small tumor cell clusters that detach from the central tumor and migrate into the stroma (Lugli et al., 2017), it would be interesting to examine whether entosis plays a role in the formation of these structures. Our analysis also revealed that the prognostic value of CIC structures in CRC arises from the strong association in stage 3 patients. However, we did not detect this association in stage 2 CRC patients who showed a lower recurrence rate (McLornan et al., 2010). Because CIC structures show a potential to be used as an independent prognostic marker, there is an urgent need to investigate the biological and clinical relevance of CIC structures in the invasive front region in other solid tumors.

Materials and methods

Reagents, antibodies, and plasmids

Dimethyl sulfoxide (#D8418), Dulbecco's PBS (#D8537), FBS (#F7525), G-418 (#04727878001), Hanks' balanced salt solution (#H8264), Hoechst 33258 (#94403), L-glutamine (#G7513), penicillin-streptomycin (#P0781), PI (#P4864), Roswell Park Memorial Institute 1640 medium (RPMI medium; #R0883), trypsin-EDTA (#T4049), and Z-Arg-Arg-AMC (#C5429) were purchased from Sigma-Aldrich. Lipofectamine 2000 (#11668019),

LysoTracker Deep Red (#L12492), LysoTracker Red (#L7528), TMRM (#T668), DRAQ5 (#65-0880-96), Alexa Fluor 488 and 647 secondary antibodies (#A11008, #A11029, #A21202, #A21206, #A31571, #A31573), and β -catenin antibody (#RB-9035) were obtained from Thermo Fisher Scientific. TRAIL (#310-04) was from PeproTech. SiR-Hoechst (#SC007) was purchased from tebu-bio. Y-27632 (#S1049), z-VAD-fmk (#S7023), and z-IETD-fmk (#S7314) were from Selleckchem. LC3A/B (#4108) and cleaved caspase-3 (#9661) antibodies were purchased from Cell Signaling Technology. Cytochrome c (#556432) antibody was from BD Biosciences. EM goat anti-rabbit IgG (#EM.GAR10) was purchased from BBI Solutions. Lamp1-mScarlet-I was a gift from Dorus Gadella (University of Amsterdam, Amsterdam, the Netherlands; Addgene plasmid #98827). pSCAT8 (CFP-IETD-Venus) was previously generated by our group (Hellwig et al., 2008). Concentrations of drugs and inhibitors used in the experiments are as follows unless otherwise mentioned: TRAIL, 10 or 100 ng/ml; CHX, 1–2 μ g/ml; z-IETD-fmk, 25 μ M; z-VAD-fmk, 25 or 50 μ M; and Y-27632, 20 μ M.

Cell culture and transfections

HCT116 cells were cultured in RPMI medium supplemented with 10% FBS, 2 mM L-glutamine, 100 U/ml penicillin, and 100 μ g/ml streptomycin at 37°C in a humidified atmosphere at 5% CO₂. Cells were cultured in six-well plates until they reached ~70% confluency and then transfected with 0.6 μ g of plasmid DNA (Venus) and 6 μ l of Lipofectamine 2000 in 1 ml Opti-MEM at 37°C with 5% CO₂ for 4–12 h. To generate stable cell lines, transfected cells were cultured in the presence of 0.5–1 mg/ml G-418 for 1–2 wk, and fluorescent clones were picked and expanded. For the generation of the stable HCT116 Lamp1-mScarlet-I cell line, cells were transfected with 0.75 μ g of plasmid DNA (Lamp1-mScarlet-I) and 7.5 μ l of Lipofectamine 2000 in 1 ml Opti-MEM. HCT116 BAX^{-/-} BAK^{-/-} (Wang and Youle, 2012) cells and their WT were a gift from Richard J. Youle (National Institutes of Health, Bethesda, MD), HCT116 caspase-8 CRISPR/Cas9 knockout cells and their WT (Henry and Martin, 2017) were a gift from S.J. Martin. HCT116 DR4^{-/-} DR5^{-/-} cells and their WT (Dufour et al., 2017) were a gift from Olivier Micheau (Centre Georges-François Leclerc, Dijon, France). Cell lines were authenticated before the beginning of the study and after completion of the experiments and regularly checked for mycoplasma.

Live cell time-lapse microscopy and FRET measurements

Cells were seeded on sterile 12-mm glass-bottom WillCo-dishes (WillCo Wells B.V.) and allowed to adhere overnight in RPMI medium at 37°C with 5% CO₂. Cells were then incubated in staining medium containing a combination of 1 μ g/ml Hoechst 33258 or 1 nM SiR-Hoechst or 1 μ M DRAQ5, 30 nM TMRM, 50 nM LysoTracker Green, LysoTracker Red, or LysoTracker Deep Red, depending on the experiment. WillCo-dishes containing stained cells were covered with embryo-tested sterile mineral oil and mounted on an LSM 710 confocal laser scanning microscope (Carl Zeiss Ltd.) equipped with a 40 \times /1.3 NA Plan Apochromat oil immersion objective and a microscope incubator chamber (37°C with 5% CO₂; Pecon) or Zeiss Axiovert 200 M automated epifluorescence microscope equipped with an Andor DU-897 BV

back-illuminated electron-multiplying charge-coupled device, 20×/0.5 NA Plan Neofluar objective, and a microscope incubator chamber. On the LSM 710, UV or cyan fluorescence was excited using 405-nm (detection range, 415–494 nm or 450–505 nm, respectively), green or yellow fluorescence was excited using 488-nm (detection range, 490–544 nm or 505–560 nm, respectively), red fluorescence was excited using 561-nm (detection range, 590–644 nm), and far-red fluorescence was excited using 633-nm (detection range, 638–728 nm) lasers. Images were recorded at a resolution of 1,024 × 1,024 pixels at zoom 1 for 16–72 h with 4–20-min intervals. On the automated epifluorescence microscope, images were recorded at a resolution of 512 × 512 pixels. Fluorescent proteins and dyes were detected using the appropriate single bandpass filter sets (Semrock). For all live cell experiments, treatments were added after ~30 min of the baseline measurement. Cell fates were determined from time-lapse microscopy images of differential interference contrast (DIC) and Hoechst recorded for 48 h. Image processing (background subtraction, median filtering, mask creation, ratiometric calculations) was performed using Fiji/ImageJ v1.52i software (National Institutes of Health). Kinetics of single-cell IETD substrate cleavage were analyzed by combining time-lapse ratiometric imaging data generated by dividing CFP by FRET after background subtraction.

HCS

Imaging

Cells were seeded on 96-well optical-bottom plates (#165305; Thermo Fisher Scientific) at a density of 7,500 cells/well, allowed to adhere overnight in RPMI medium at 37°C with 5% CO₂, and then stained with Hoechst (1 μg/ml), PI (1 μg/ml), and LysoTracker Deep Red (50 nM) as indicated. The dyes were present in the medium throughout the experiment. 96-well plates containing stained cells were treated in triplicate as indicated in the figure legends and imaged using Cellomics ArrayScan VTi (Thermo Fisher Scientific) equipped with a 10×/0.45 NA Plan Apochromat objective lens, multidiode light source (SOLA SE II; Lumencor) set to 20%–22% of maximal emission intensity, and a monochrome charge-coupled device camera (Orca-AG; Hamamatsu). Time series of images (12 fields of view per well) were collected from each well for 72 h, with 6-h intervals, at a resolution of 1,024 × 1,024 pixels. Dye concentrations and image acquisition rate were optimized in advance to minimize phototoxicity. Hoechst was imaged using 100-ms exposure time, a 381–394-nm excitation filter, and a 415–460-nm emission filter; CFP was imaged using 1,000-ms exposure time, a 422–432-nm excitation filter, and a 457–487-nm emission filter; FRET was imaged using 300-ms exposure time, a 422–432-nm excitation filter, and a 528–555-nm emission filter; PI was imaged using 75-ms exposure time, a 582–596-nm excitation filter, and a 608–683-nm emission filter; and LysoTracker Deep Red was imaged using 500-ms exposure time, a 644–657-nm excitation filter, and a 690–730-nm emission filter. The autofocus module on Cellomics ArrayScan was applied on the FRET channel in every third field of view at 4 × 4 binning.

Image processing and analysis

All images were segmented and measured using CellProfiler 2.2 (Broad Institute). We optimized and combined modules for

uneven/nonuniform background illumination correction, nuclei isolation, and shape/intensity parameter identification to create an HCS image processing and analysis workflow. The data obtained was further processed using Excel 2016 (Microsoft Corporation). The multiplexing of Venus, Hoechst, PI, and LysoTracker Deep Red staining allows the automated identification of specific cell states. These include cells that exhibit caspase-8-like activity (FRET disruption caused by IETD cleavage), cells showing an apoptotic nuclear morphology (PI-negative small and fragmented nuclei), dead cells (PI positive), and late entotic cells (bright LysoTracker Deep Red stain that colocalized with Hoechst stain). Because we were not able to automatically identify early entotic cells, they were manually quantified based on detecting round-shaped Hoechst-stained cells inside a large vacuole within another Hoechst-stained cell showing a crescent-shaped nuclear morphology.

Entosis quantification

Cells were seeded, stained, and treated on sterile 12-mm glass-bottom WillCo-dishes in RPMI medium at 37°C with 5% CO₂. Entosis events were determined by counting at least 500 cells/sample by either using time-lapse microscopy images or 3D confocal microscopy of immunofluorescence staining (Hoechst and β-catenin) after 48 h of treatment. Events were quantified based on detecting round-shaped (Hoechst-stained) cells inside a large vacuole within another (Hoechst-stained) cell showing a crescent-shaped nuclear morphology. Both dead and alive inner cells were quantified as entotic.

Immunofluorescence staining and 3D confocal imaging

Cells were seeded on sterile 12-mm glass-bottom WillCo-dishes and allowed to adhere overnight in RPMI medium at 37°C with 5% CO₂. Cells were then treated for indicated times and fixed in 4% paraformaldehyde diluted in PBS for 15 min at room temperature. For experiments shown in Fig. 3, A and B, LysoTracker Deep Red was added 30 min before fixation. After washing three times in 1× PBS for 5 min each, cells were blocked in a blocking buffer (1× PBS, 5% normal goat serum, and 0.3% Triton X-100) for 60 min. Primary antibodies were prepared in a dilution buffer (1× PBS, 1% BSA, 0.3% Triton X-100), and samples were incubated overnight at 4°C. For double immunofluorescence staining, a mixture of two primary antibodies from different species were simultaneously added. After washing three times in 1× PBS for 5 min each, complementary secondary antibodies (different fluorochromes were used for double immunofluorescence staining) were prepared in a dilution buffer, and cells were incubated for 2 h at room temperature in the dark. Samples were washed in 1× PBS for 5 min each, stained with 2 μg/ml for 10 min, and washed once with 1× PBS. Samples were then mounted on an LSM 710 confocal laser-scanning microscope (Carl Zeiss) fitted with a 63×/1.4 NA Plan Apochromat oil immersion objective. 405-, 488-, 561-, and 633-nm lasers were used to excite DAPI and Alexa Fluor 488, 561, and 647-conjugated secondary antibodies with detection ranges of 415–494, 490–544, 560–628, and 638–728 nm, respectively. Z-stacks were taken by recording a series of optical slices with an optimal thickness (0.6–1 μm) at 1,024 × 1,024 or 2,048 × 2,048 pixels throughout

the entire cells. Further image processing (background subtraction, median filtering, and construction of orthogonal views) and quantification were performed using Fiji/ImageJ v1.52i software. For experiments shown in Fig. 1 K, mean intensity values for outer cells were normalized to mean intensity values of apoptotic cells recorded from the same field of view. For experiments shown in Fig. S3 C, mean intensity values for inner cells were normalized to the average of five neighboring cells from the same field of view.

Cell internalization assay

Cells were seeded in six-well plates at a density of 500,000 cells/well and allowed to adhere overnight in RPMI medium at 37°C with 5% CO₂. The next day, cells were stained with CellTracker Green (#C2925; Thermo Fisher Scientific) or CellTracker Red (#C34552, Thermo Fisher Scientific) for 30 min in prewarmed serum-free RPMI medium. Stained green and red cells were washed three times with PBS and trypsinized to obtain single-cell suspension. Green and red cells were then stained with Hoechst and mixed with or without z-VAD-fmk or Y-27632 for 1 h. Mixed cells were plated onto 96-well optical-bottom plates with or without TRAIL in the absence or presence of z-VAD-fmk or Y-27632 for 24 h. Images were recorded by HCS autofocusing on the Hoechst channel. Imaging was performed using a 20×/0.5 NA objective and quad band beam splitter and emission filter (from F66-888; Semrock) in combination with selective excitation for Hoechst (381–394 nm for 250 ms), CellTracker Green (475–495 nm excitation, 500–550 nm emission), and CellTracker Red (547–573 nm excitation, 608–682 nm emission), both for 100 ms using the full resolution of the Orca-AG camera. Images were analyzed manually after processing with CellProfiler v2.2 and Fiji/ImageJ v1.52i software, as explained above and in Fig. 4 G.

Cathepsin B activity

Cells were seeded on sterile 12-mm glass-bottom WillCo-dishes and allowed to adhere overnight in RPMI medium at 37°C with 5% CO₂. After treatments, Z-Arg-Arg-AMC, the fluorogenic substrate for cathepsin B, was added to the media at a concentration of 50 μM. Cells were fixed in 4% paraformaldehyde or imaged alive on an LSM 710 confocal laser-scanning microscope (Carl Zeiss) as described above.

CLEM analysis

Cells were seeded on 35-mm sterile high Grid-500 μ-Dishes (ibidi GmbH), allowed to adhere overnight in RPMI medium at 37°C with 5% CO₂, and then treated with TRAIL for 48 h. After staining with LysoTracker for 30 min, cells were immediately fixed in 4% paraformaldehyde and stained with Hoechst. 3D confocal imaging of DIC, Hoechst, and LysoTracker staining was performed as described above, and areas containing entosis events were recorded for further analysis. Samples were then fixed again in 2.5% glutaraldehyde in sodium cacodylate buffer and then washed three times in cacodylate buffer. After fixation, samples were placed in 1% osmium in sodium cacodylate buffer for 60 min and then rinsed three times in distilled water. Next, samples were incubated in increasing concentrations of methanol (50%, 60%, 70%, 80%, 90%, 95%, 100%, 100%). Subsections

of interest (SOIs) were isolated from the samples using a scalpel and placed in LR white resin prepared in methanol (1:1 ratio) for 60 min, followed by LR white resin only for another 60 min. SOIs were then embedded in fresh LR white resin using a gelatin capsule and incubated overnight under UV light at 4°C. Ultramicrotome sections at 60–90-nm thickness were generated using a Leica EM UC6 (Laboratory Instruments and Supplies) and trapped on pioloform-coated 3-mm 200-thin bar copper grids. Images of the events of interest were recorded using a Hitachi H-7650 TEM at an accelerating voltage of 40–100 kV. Enhance Local Contrast (CLAHE) plugin in Fiji/ImageJ v1.52i software was used to automatically enhance the contrast of images shown in Fig. 3, C–E.

Light sheet fluorescence microscopy

Sample preparation

HCT116 cells were seeded on 96-well spheroid plates (96-well Black/Clear Round Bottom Ultra-Low Attachment Spheroid Microplate; Corning) at a density of 1,000 cells/well and grown in RPMI medium at 37°C with 5% CO₂ for 48 h until they formed spheres. To stain the spheres homogenously, stains were added to the spheroid culture as indicated for at least 5 h at the following concentrations: LysoTracker Red, 50 nM; LysoTracker Deep Red, 10 nM; SiR-Hoechst, 0.5 μM; and Hoechst, 33258 1 μg/ml.

Imaging

The spheroids were embedded in 1% low melting agarose in PBS (Sigma-Aldrich) at 38°C–40°C and sucked into a glass capillary while liquid. When hardened, the capillary was mounted in the microscope sample holder and chamber of the light sheet fluorescence microscope (Lightsheet Z1; Carl Zeiss) using glass capillaries with an inner diameter of 1.0 mm and outer diameter of 1.5 mm. A plunger was then used to push the agar with the embedded spheroids out of the capillary into the liquid in front of the 20×/1.0 NA lens. The light sheet was generated with two 10×/0.2 NA lenses illuminating the sample, alternating from each side using the pivot scan mode. Images were taken at zoom 1.0–1.3 using a light sheet thickness from 3.61 μm to 4.11 μm, respectively (405-nm excitation). Hoechst 33258 was excited using the 405-nm laser line, the Venus component of the IETD FRET probe with 488 nm, LysoTracker Red with 561 nm, and SiR-Hoechst with 638 nm, all using the 405/488/561/640-nm notch filter in the emission light path to block scattered laser light. Emission was split onto the two pco.edge scientific complementary metal-oxide-semiconductor cameras using filter cubes with beam splitter 1 at 490 nm using bandpass filters of 420–470 nm (Hoechst/CFP) and 505–545 nm (FRET), beam splitter 2 at 510 nm using a bandpass filter of 575–615 nm (LysoTracker Red), and beam splitter 3 at 560 nm using a bandpass filter of 505–545 nm (Venus) and a long pass filter of 660 nm (SiR-Hoechst). Image stacks were then taken while moving the object along the optical axis of the imaging objective at 1-μm steps and subsequently turning the object in 45° steps and realigning the object for each of the next four stacks. All images were processed using ZEN black and Fiji/ImageJ v1.52r-t software. The multiview fusion and deconvolution were performed using the dedicated Fiji plugins (MultiView Reconstruction

v5.0.20; [Preibisch et al., 2010](#)) with either using Hoechst-stained nuclei or LysoTracker-stained lysosomes as an alignment aid for registration. For the image fusion processing, the scale was set to 2 \times using a server with dual Xeon Gold and 192-GB RAM (Power Edge R 740 XD; Dell EMC); deconvolution was done with a 512-pixel³ block size.

Immunogold labeling

Following TEM analysis, grids were incubated in a drop of blocking buffer (0.1% Tween 20, 2% goat serum, 2% BSA in PBS) for 30 min at room temperature. After blocking, grids were placed in a drop containing LC3 primary antibody (1:100) for overnight at 4°C. Next, grids were washed in a drop of PBS for 1 h (4 \times 15 min). Following washing, grids were incubated in a drop of secondary antibody conjugated to 10-nm gold particles (1:50) for 1 h at room temperature. Grids were washed in PBS for 25 min (5 \times 5 min) and immediately imaged using a Hitachi H-7650 TEM. Antibodies used in immunogold labeling were diluted in blocking buffer.

Western blot

Protein lysates were isolated using radioimmunoprecipitation assay buffer (140 mM NaCl, 10 mM Tris-HCl [pH 8.0], 1 mM EDTA, 1% Triton X-100, 0.1% sodium deoxycholate, 0.1% SDS) with freshly added protease and phosphatase inhibitors and quantified using Pierce BCA Protein Assay Kit (#23227; Thermo Fisher Scientific). Proteins were separated by SDS-PAGE and blotted using a semi-dry transfer blotter (Power Blotter XL System, #PB0013; Invitrogen). Anti-Pro Caspase-8 (#ab108333) was purchased from Abcam. Anti-DR4 (#42533), anti-DR5 (#8074), and anti-Bax (#2772) were purchased from Cell Signaling Technology. Anti-Bak (#sc-832) was purchased from Santa Cruz Biotechnology and used at 1:1,000 dilution. Anti- β -actin (#A5441) was purchased from Sigma-Aldrich and used at 1:5,000 dilution. HRP-conjugated anti-mouse (#AP124P) and anti-rabbit (#AP132P) antibodies were purchased from Sigma-Aldrich and used at 1:5,000 dilution. The signal was developed using Immobilon Western Chemiluminescent HRP Substrate (#WBKLS0500; Merck), and images were taken by a Fujifilm LAS-4000 imaging system.

Immunohistochemistry

Immunohistochemistry was performed on a Ventana Benchmark XT automated immunostainer (Roche Diagnostics). c-MET staining was conducted according to the manufacturer's instructions using the Ventana CONFIRM c-MET Rabbit Monoclonal Antibody (SP44, #790-4430). The antibody was prediluted ready to use and dispensed neat with an incubation of 16 min on the slide, following cell conditioning solution 1 heat-induced epitope retrieval of the tissue for 60 min. Antibody binding was visualized with DAB chromogen (Ventana ultraView Universal DAB Detection Kit, cat. no. 760-500). c-MET immunohistochemistry expression was validated and evaluated for sensitivity and specificity on CRC control material demonstrating a range of expression and was visually reviewed by a Fellow of the Royal College of Pathologists clinical diagnostician. Slide scanning was conducted at \times 40 magnification using a Leica Aperio AT2 scanner.

Analysis of CIC structures in CRC tissue microarrays

Patients cohort

Patients were drawn down from the NI240 phase III clinical trial coordinated at Queen's University where primarily stage 2 and 3 CRC patients were randomly assigned to observation or adjuvant treatment with 5-FU/leucovorin following primary tumor resection ([McLornan et al., 2010](#)). Clinicopathological characteristics, including treatment randomization, TNM staging, tumor location, lymphovascular invasion, and outcome were annotated for 240 patients who met the inclusion criteria. Patients were followed-up after surgery for \sim 7 yr.

TMA

Tissues from the tumor center, the invasive front, and matched normal mucosa were collected during surgical resection and preserved in formalin-fixed paraffin-embedded blocks for the construction of TMAs ([McLornan et al., 2010](#)). Multiple TMA cores per patient (two cores for the invasive front and up to six cores for normal and tumor center) were stained for H&E and hematoxylin/c-MET, totaling 2,791 cores in 232 patients. CIC structures that exhibited evidence of a complete internalization of an entire cell were manually quantified by independently detecting at least four of the five following criteria: (1) nucleus of inner cell, (2) cytoplasm of inner cell, (3) a crescent-shaped nucleus of outer cell, (4) cytoplasm of outer cell, and (5) visible vacuolar space between inner and outer cells. Events identified as CIC structures were recorded using QuPath v0.2.0-m2 ([Bankhead et al., 2017](#)). Moreover, multiple TMA cores ($n = 7,601$) from tumor center and matched normal tissue were stained for TRAIL, TRAIL-R1 (DR4), TRAIL-R2 (DR5), caspase-8, and c-FLIP for 236 patients. Protein expression was computed as previously described ([McLornan et al., 2010](#)) as the product of the staining scores for intensity (0–3 integer scale) and coverage (0–4 integer scale), with low and high values indicating weak and strong expression, respectively.

In downstream analysis, we included 220 patients with annotated clinical records and CIC structures in at least a tissue type. Additional analysis examining the association between CIC structures and protein profiles was possible in 220 patients with material to quantify the proteins. Data and analysis codes are publicly available and archived at Zenodo at <https://zenodo.org/record/3841833>.

Statistical analysis

In vitro data

When comparing groups containing single-cell information, data obtained from three experiments were presented as individual values for each cell as well as median and quartiles in each group by violin plots. When comparing groups containing a value per experiment, data were presented as individual values for each experiment as well as the SEM in each group by aligned dot plots with bars. Statistical significance between the means of two groups was tested using unpaired two-tailed *t* test and among the means of more than two groups, was tested using one-way ANOVA followed by Tukey's multiple comparison test. GraphPad Prism 9 software was used to perform statistical comparison tests and preparation of graphs. Figures were

prepared using Adobe Illustrator version CS6 software. Asterisks represent significance with *, $P < 0.05$; **, $P < 0.01$; ***, $P < 0.001$; and ****, $P < 0.0001$. All experiments were repeated at least three times unless otherwise indicated.

Clinical data

CIC events analysis. Agreement between CIC events (median across biological replicas per tissue per patient) estimated from H&E or c-MET staining was assessed by Kendall rank correlation τ (Python package *scipy* v1.2.0). We analyzed the association between CIC events by tissue and clinical covariates with zero-inflated Poisson regression models, including a random effect for each patient and covariate fixed effects. We reported effect sizes (estimate), 95% CIs, and P values computed by likelihood ratio tests (R package *glmmTMB* v1.0.0-1).

Protein expression analysis. Protein expression across biological replicas per tissue and per patient was aggregated by the median. Association between protein expression and CIC events (binary, CIC = 0 versus CIC > 0) was assessed in tumor tissue by unadjusted linear models.

Outcome analysis

We examined DFS and DSS as outcome end points. DFS, DSS, and overall survival were computed as the time interval between surgical resection and either study end date or end point event (tumor recurrence as evidenced by radiological imaging or cancer-related death, respectively). Patients with no events were censored at study end date. Differences in survival curves between patient groups were assessed by Kaplan–Meier estimates and log-rank tests. We investigated the association between CIC structures (absence [CIC = 0] versus presence [CIC > 0]) with the outcome by univariate and multivariate Cox regression hazard models. The multivariate model was adjusted by baseline patient characteristics selected a priori, including stage (2 versus 3), treatment (observation versus 5-FU/leucovorin), age (continuous), sex (male versus female), and tumor location (colon versus rectum). We reported HRs, 95% CIs, and P values computed by log-likelihood ratio tests. Survival analyses were performed in Python with the *lifelines* package v0.24.0 (Davidson-Pilon, 2019).

Asterisks represent significance with *, $P < 0.05$; **, $P < 0.01$; ***, $P < 0.001$; and ****, $P < 0.0001$ between groups in the figures. P values were not adjusted for multiple comparisons as these analyses were deemed exploratory.

Online supplemental material

Figure S1 shows examples of entotic structures during long-term time lapse microscopy in TRAIL-stimulated cells. Figure S2 shows representative images and manual quantification of entotic structures in HCT116, MCF-7, and LS180 cells as well as HCT116 spheroids with or without TRAIL treatment. Figure S3 shows ultrastructural localization of LC3 in negative control and middle-stage inner cell shown in Fig. 3. Figure S4 shows representative fields of view and quantification of cells with cleaved IETD substrate in HCT116 cells treated with or without TRAIL in the absence or presence of Y-27632 or caspase inhibitors. Figure S5 shows an overview of clinical, demographic, pathological, and

molecular information for the CRC patients of the NI240 phase III clinical trial. Video 1 shows HCT116 IETD cells showing formation of apoptotic and entotic structures in response to TRAIL treatment. Video 2 shows HCT116 cells showing surviving and dying entotic cells in response to TRAIL treatment. Video 3 shows a 3D projection of an inner cell showing LysoTracker accumulation during entosis. Video 4 shows that reduction of Venus signal coincides with accumulation of TMRM and LysoTracker in inner cells during entotic cell death. Video 5 shows a 3D projection of HCT116 IETD spheroids showing entotic structures in control and TRAIL treatment. Video 6 shows lysosomal events during entotic cell death in TRAIL-treated cells. Video 7 shows release of inner cells in HCT116 *Bax*^{-/-} *Bac*^{-/-} during TRAIL treatment. Table S1 summarizes clinical, demographic, and pathological characteristics of the patients. Table S2 shows the association between CIC events detected in TMA sections and clinical, demographic, or pathological covariates by tissue type.

Acknowledgments

We thank Prof. Olivier Micheau and Dr. Abdelmonim Radua (Centre Georges-François Leclerc, Dijon, France) for providing HCT116 DR4^{-/-} DR5^{-/-} cells and their WT counterparts. We also thank the NI240 study participants and trial investigators.

This study was supported by Science Foundation Ireland (14/IA/2582, 16/RI/3740, 16/US/3301) and the Health Research Board (16/US/330, TRA/2007/26). This research was funded in whole or in part by Science Foundation Ireland. For the purpose of Open Access, the author has applied a CC-BY public copyright license to any Author Accepted Manuscript (AAM) version arising from this submission.

The authors declare no competing financial interests.

Author contributions: Conceptualization: E. Bozkurt, H. Düsselmann, and J.H.M. Prehn. Methodology: E. Bozkurt, H. Düsselmann, B.L. Cavanagh, and M. Salvucci. Formal analysis: E. Bozkurt, H. Düsselmann, and M. Salvucci. Investigation: E. Bozkurt, H. Düsselmann, and M. Salvucci. Resources: J.H.M. Prehn, S. Van Schaeybroeck, D.B. Longley, and S.J. Martin. Writing-original draft: E. Bozkurt. Writing-review and editing: H. Düsselmann, M. Salvucci, S. Van Schaeybroeck, D.B. Longley, S.J. Martin, and J.H.M. Prehn. Visualization: E. Bozkurt and M. Salvucci. Supervision: J.H.M. Prehn. Funding acquisition: D.B. Longley and J.H.M. Prehn.

Submitted: 7 October 2020

Revised: 14 July 2021

Accepted: 31 August 2021

References

- Bankhead, P., M.B. Loughrey, J.A. Fernández, Y. Dombrowski, D.G. McArt, P.D. Dunne, S. McQuaid, R.T. Gray, L.J. Murray, H.G. Coleman, et al. 2017. QuPath: Open source software for digital pathology image analysis. *Sci. Rep.* 7:16878. <https://doi.org/10.1038/s41598-017-17204-5>
- Brooks, A.D., and T.J. Sayers. 2005. Reduction of the antiapoptotic protein cFLIP enhances the susceptibility of human renal cancer cells to TRAIL apoptosis. *Cancer Immunol. Immunother.* 54:499–505. <https://doi.org/10.1007/s00262-004-0595-8>

- Davidson-Pilon, C. 2019. lifelines: survival analysis in Python. *JOSS*. 4:1317. <https://doi.org/10.21105/joss.01317>
- de Looft, M., S. de Jong, and F.A.E. Kruyt. 2019. Multiple interactions between cancer cells and the tumor microenvironment modulate TRAIL signaling: Implications for TRAIL receptor targeted therapy. *Front. Immunol.* 10:1530. <https://doi.org/10.3389/fimmu.2019.01530>
- de Miguel, D., J. Lemke, A. Anel, H. Walczak, and L. Martinez-Lostao. 2016. Onto better TRAILs for cancer treatment. *Cell Death Differ.* 23:733-747. <https://doi.org/10.1038/cdd.2015.174>
- Dufour, F., T. Rattier, A.A. Constantinescu, L. Zischler, A. Morlé, H.B. Mabrouk, E. Humblin, G. Jacquemin, E. Szegezdi, F. Delacote, et al. 2017. TRAIL receptor gene editing unveils TRAIL-R1 as a master player of apoptosis induced by TRAIL and ER stress. *Oncotarget*. 8:9974-9985. <https://doi.org/10.18632/oncotarget.14285>
- Durgan, J., Y.-Y. Tseng, J.C. Hamann, M.-C. Domart, L. Collinson, A. Hall, M. Overholtzer, and O. Florey. 2017. Mitosis can drive cell cannibalism through entosis. *eLife*. 6:e27134. <https://doi.org/10.7554/eLife.27134>
- Falschlehner, C., C.H. Emmerich, B. Gerlach, and H. Walczak. 2007. TRAIL signalling: Decisions between life and death. *Int. J. Biochem. Cell Biol.* 39:1462-1475. <https://doi.org/10.1016/j.biocel.2007.02.007>
- Fitzwalter, B.E., C.G. Towers, K.D. Sullivan, Z. Andrysik, M. Hoh, M. Ludwig, J. O'Prey, K.M. Ryan, J.M. Espinosa, M.J. Morgan, and A. Thorburn. 2018. Autophagy inhibition mediates apoptosis sensitization in cancer therapy by relieving FOXO3a turnover. *Dev. Cell*. 44:555-565.e3. <https://doi.org/10.1016/j.devcel.2018.02.014>
- Florey, O., S.E. Kim, C.P. Sandoval, C.M. Haynes, and M. Overholtzer. 2011. Autophagy machinery mediates macroendocytic processing and entotic cell death by targeting single membranes. *Nat. Cell Biol.* 13:1335-1343. <https://doi.org/10.1038/ncb2363>
- Flusberg, D.A., and P.K. Sorger. 2013. Modulating cell-to-cell variability and sensitivity to death ligands by co-drugging. *Phys. Biol.* 10:035002. <https://doi.org/10.1088/1478-3975/10/3/035002>
- Flusberg, D.A., J. Roux, S.L. Spencer, and P.K. Sorger. 2013. Cells surviving fractional killing by TRAIL exhibit transient but sustainable resistance and inflammatory phenotypes. *Mol. Biol. Cell*. 24:2186-2200. <https://doi.org/10.1091/mbc.e12-10-0737>
- Fulda, S. 2013. The dark side of TRAIL signaling. *Cell Death Differ.* 20:845-846. <https://doi.org/10.1038/cdd.2013.36>
- Garanina, A.S., O.P. Kisurina-Evgenieva, M.V. Erokhina, E.A. Smirnova, V.M. Factor, and G.E. Onishchenko. 2017. Consecutive entosis stages in human substrate-dependent cultured cells. *Sci. Rep.* 7:12555. <https://doi.org/10.1038/s41598-017-12867-6>
- Green, D.R. 2011. Means to an End: Apoptosis and Other Cell Death Mechanisms. Cold Spring Harbor Laboratory Press, Cold Spring Harbor, NY.
- Guseva, N.V., O.W. Rokhlin, A.F. Taghiyev, and M.B. Cohen. 2008. Unique resistance of breast carcinoma cell line T47D to TRAIL but not anti-Fas is linked to p43cFLIP(L). *Breast Cancer Res. Treat.* 107:349-357. <https://doi.org/10.1007/s10549-007-9563-2>
- Hamann, J.C., A. Surcel, R. Chen, C. Teragawa, J.G. Albeck, D.N. Robinson, and M. Overholtzer. 2017. Entosis is induced by glucose starvation. *Cell Rep.* 20:201-210. <https://doi.org/10.1016/j.celrep.2017.06.037>
- Hartwig, T., A. Montinaro, S. von Karstedt, A. Sevko, S. Surinova, A. Chakravarthy, L. Taraborrelli, P. Draber, E. Lafont, F. Arce Vargas, et al. 2017. The TRAIL-induced cancer secretome promotes a tumor-supportive immune microenvironment via CCR2. *Mol. Cell*. 65:730-742.e5. <https://doi.org/10.1016/j.molcel.2017.01.021>
- Hellwig, C.T., B.F. Kohler, A.-K. Lehtivarjo, H. Dussmann, M.J. Courtney, J.H.M. Prehn, and M. Rehm. 2008. Real time analysis of tumor necrosis factor-related apoptosis-inducing ligand/cycloheximide-induced caspase activities during apoptosis initiation. *J. Biol. Chem.* 283:21676-21685. <https://doi.org/10.1074/jbc.M802889200>
- Henry, C.M., and S.J. Martin. 2017. Caspase-8 Acts in a non-enzymatic role as a scaffold for assembly of a pro-inflammatory "FADDosome" complex upon TRAIL stimulation. *Mol. Cell*. 65:715-729.e5. <https://doi.org/10.1016/j.molcel.2017.01.022>
- Kerr, J.F.R., A.H. Wyllie, and A.R. Currie. 1972. Apoptosis: A basic biological phenomenon with wide-ranging implications in tissue kinetics. *Br. J. Cancer*. 26:239-257. <https://doi.org/10.1038/bjc.1972.33>
- Koelzer, V.H., I. Zlobec, and A. Lugli. 2016. Tumor budding in colorectal cancer--ready for diagnostic practice? *Hum. Pathol.* 47:4-19. <https://doi.org/10.1016/j.humpath.2015.08.007>
- Krishna, S., and M. Overholtzer. 2016. Mechanisms and consequences of entosis. *Cell. Mol. Life Sci.* 73:2379-2386. <https://doi.org/10.1007/s00018-016-2207-0>
- Lin, C.-Y., T.-W. Chang, W.-H. Hsieh, M.-C. Hung, I.-H. Lin, S.-C. Lai, and Y.-J. Tzeng. 2016. Simultaneous induction of apoptosis and necroptosis by Tanshinone IIA in human hepatocellular carcinoma HepG2 cells. *Cell Death Discov.* 2:16065. <https://doi.org/10.1038/cddiscovery.2016.65>
- Lugli, A., R. Kirsch, Y. Ajioka, F. Bosman, G. Cathomas, H. Dawson, H. El Zimaity, J.-F. Fléjou, T.P. Hansen, A. Hartmann, et al. 2017. Recommendations for reporting tumor budding in colorectal cancer based on the International Tumor Budding Consensus Conference (ITBCC) 2016. *Mod. Pathol.* 30:1299-1311. <https://doi.org/10.1038/modpathol.2017.46>
- Mackay, H.L., D. Moore, C. Hall, N.J. Birkbak, M. Jamal-Hanjani, S.A. Karim, V.M. Phatak, L. Piñon, J.P. Morton, C. Swanton, et al. 2018. Genomic instability in mutant p53 cancer cells upon entotic engulfment. *Nat. Commun.* 9:3070. <https://doi.org/10.1038/s41467-018-05368-1>
- Martins, I., S.Q. Raza, L. Voisin, H. Dakhli, A. Allouch, F. Law, D. Sabino, D. De Jong, M. Thoreau, E. Mintet, et al. 2018. Anticancer chemotherapy and radiotherapy trigger both non-cell-autonomous and cell-autonomous death. *Cell Death Dis.* 9:716. <https://doi.org/10.1038/s41419-018-0747-y>
- McLornan, D.P., H.L. Barrett, R. Cummins, U. McDermott, C. McDowell, S.J. Conlon, V.M. Coyle, S. Van Schaevebroeck, R. Wilson, E.W. Kay, et al. 2010. Prognostic significance of TRAIL signaling molecules in stage II and III colorectal cancer. *Clin. Cancer Res.* 16:3442-3451. <https://doi.org/10.1158/1078-0432.CCR-10-0052>
- Moriwaki, K., K. Noda, Y. Furukawa, K. Ohshima, A. Uchiyama, T. Nakagawa, N. Taniguchi, Y. Daigo, Y. Nakamura, N. Hayashi, and E. Miyoshi. 2009. Deficiency of GMDS leads to escape from NK cell-mediated tumor surveillance through modulation of TRAIL signaling. *Gastroenterology*. 137:188-198.e2. <https://doi.org/10.1053/j.gastro.2009.04.002>
- Overholtzer, M., and J.S. Brugge. 2008. The cell biology of cell-in-cell structures. *Nat. Rev. Mol. Cell Biol.* 9:796-809. <https://doi.org/10.1038/nrm2504>
- Overholtzer, M., A.A. Mailleux, G. Mouneimne, G. Normand, S.J. Schnitt, R.W. King, E.S. Cibas, and J.S. Brugge. 2007. A nonapoptotic cell death process, entosis, that occurs by cell-in-cell invasion. *Cell*. 131:966-979. <https://doi.org/10.1016/j.cell.2007.10.040>
- Preibisch, S., S. Saalfeld, J. Schindelin, and P. Tomancak. 2010. Software for bead-based registration of selective plane illumination microscopy data. *Nat. Methods*. 7:418-419. <https://doi.org/10.1038/nmeth0610-418>
- Reis, C.R., P.-H. Chen, N. Bendris, and S.L. Schmid. 2017. TRAIL-death receptor endocytosis and apoptosis are selectively regulated by dynamin-1 activation. *Proc. Natl. Acad. Sci. USA*. 114:504-509. <https://doi.org/10.1073/pnas.1615072114>
- Roux, J., M. Hafner, S. Bandara, J.J. Sims, H. Hudson, D. Chai, and P.K. Sorger. 2015. Fractional killing arises from cell-to-cell variability in overcoming a caspase activity threshold. *Mol. Syst. Biol.* 11:803. <https://doi.org/10.15252/msb.20145584>
- Sag, D., Z.O. Ayyildiz, S. Gunalp, and G. Wingender. 2019. The Role of TRAIL/DRs in the modulation of immune cells and responses. *Cancers (Basel)*. 11:1469. <https://doi.org/10.3390/cancers11101469>
- Schaefer, U., O. Voloshanenko, D. Willen, and H. Walczak. 2007. TRAIL: A multifunctional cytokine. *Front. Biosci.* 12:3813-3824. <https://doi.org/10.2741/2354>
- Schenker, H., M. Büttner-Herold, R. Fietkau, and L.V. Distel. 2017. Cell-in-cell structures are more potent predictors of outcome than senescence or apoptosis in head and neck squamous cell carcinomas. *Radiat. Oncol.* 12:21. <https://doi.org/10.1186/s13014-016-0746-z>
- Shinoda, H., M. Shannon, and T. Nagai. 2018. Fluorescent proteins for investigating biological events in acidic environments. *Int. J. Mol. Sci.* 19:1548. <https://doi.org/10.3390/ijms19061548>
- Sun, Q., T. Luo, Y. Ren, O. Florey, S. Shirasawa, T. Sasazuki, D.N. Robinson, and M. Overholtzer. 2014. Competition between human cells by entosis. *Cell Res.* 24:1299-1310. <https://doi.org/10.1038/cr.2014.138>
- Tonnessen-Murray, C.A., W.D. Frey, S.G. Rao, A. Shahbandi, N.A. Ungerleider, J.O. Olayiwola, L.B. Murray, B.T. Vinson, D.B. Chrisey, C.J. Lord, and J.G. Jackson. 2019. Chemotherapy-induced senescent cancer cells engulf other cells to enhance their survival. *J. Cell Biol.* 218:3827-3844. <https://doi.org/10.1083/jcb.201904051>
- van Dijk, M., A. Halpin-McCormick, T. Sessler, A. Samali, and E. Szegezdi. 2013. Resistance to TRAIL in non-transformed cells is due to multiple redundant pathways. *Cell Death Dis.* 4:e702. <https://doi.org/10.1038/cddis.2013.214>
- Wajant, H., E. Haas, R. Schwenzer, F. Mühlenbeck, S. Kreuz, G. Schubert, M. Grell, C. Smith, and P. Scheurich. 2000. Inhibition of death receptor-mediated gene induction by a cycloheximide-sensitive factor occurs at the level of or upstream of Fas-associated death domain protein (FADD). *J. Biol. Chem.* 275:24357-24366. <https://doi.org/10.1074/jbc.M000811200>
- Walczak, H. 2013. Death receptor-ligand systems in cancer, cell death, and inflammation. *Cold Spring Harb. Perspect. Biol.* 5:a008698. <https://doi.org/10.1101/cshperspect.a008698>

- Wan, Q., J. Liu, Z. Zheng, H. Zhu, X. Chu, Z. Dong, S. Huang, and Q. Du. 2012. Regulation of myosin activation during cell-cell contact formation by Par3-Lgl antagonism: Entosis without matrix detachment. *Mol. Biol. Cell.* 23:2076–2091. <https://doi.org/10.1091/mbc.e11-11-0940>
- Wang, C., and R.J. Youle. 2012. Predominant requirement of Bax for apoptosis in HCT116 cells is determined by Mcl-1's inhibitory effect on Bak. *Oncogene.* 31:3177–3189. <https://doi.org/10.1038/onc.2011.497>
- Wiley, S.R., K. Schooley, P.J. Smolak, W.S. Din, C.-P. Huang, J.K. Nicholl, G.R. Sutherland, T.D. Smith, C. Rauch, C.A. Smith, and R.G. Goodwin. 1995. Identification and characterization of a new member of the TNF family that induces apoptosis. *Immunity.* 3:673–682. [https://doi.org/10.1016/1074-7613\(95\)90057-8](https://doi.org/10.1016/1074-7613(95)90057-8)
- Zlobec, I., and A. Lugli. 2009. Invasive front of colorectal cancer: Dynamic interface of pro-/anti-tumor factors. *World J. Gastroenterol.* 15: 5898–5906. <https://doi.org/10.3748/wjg.15.5898>

Supplemental material

Tables S1 and S2 are provided online as separate Word files. Table S1 summarizes clinical, demographic, and pathological characteristics of the patients of the NI240 phase III clinical trial. Table S2 shows the association between number of observed CIC events detected in TMA sections and clinical, demographic, or pathological covariates by tissue type.

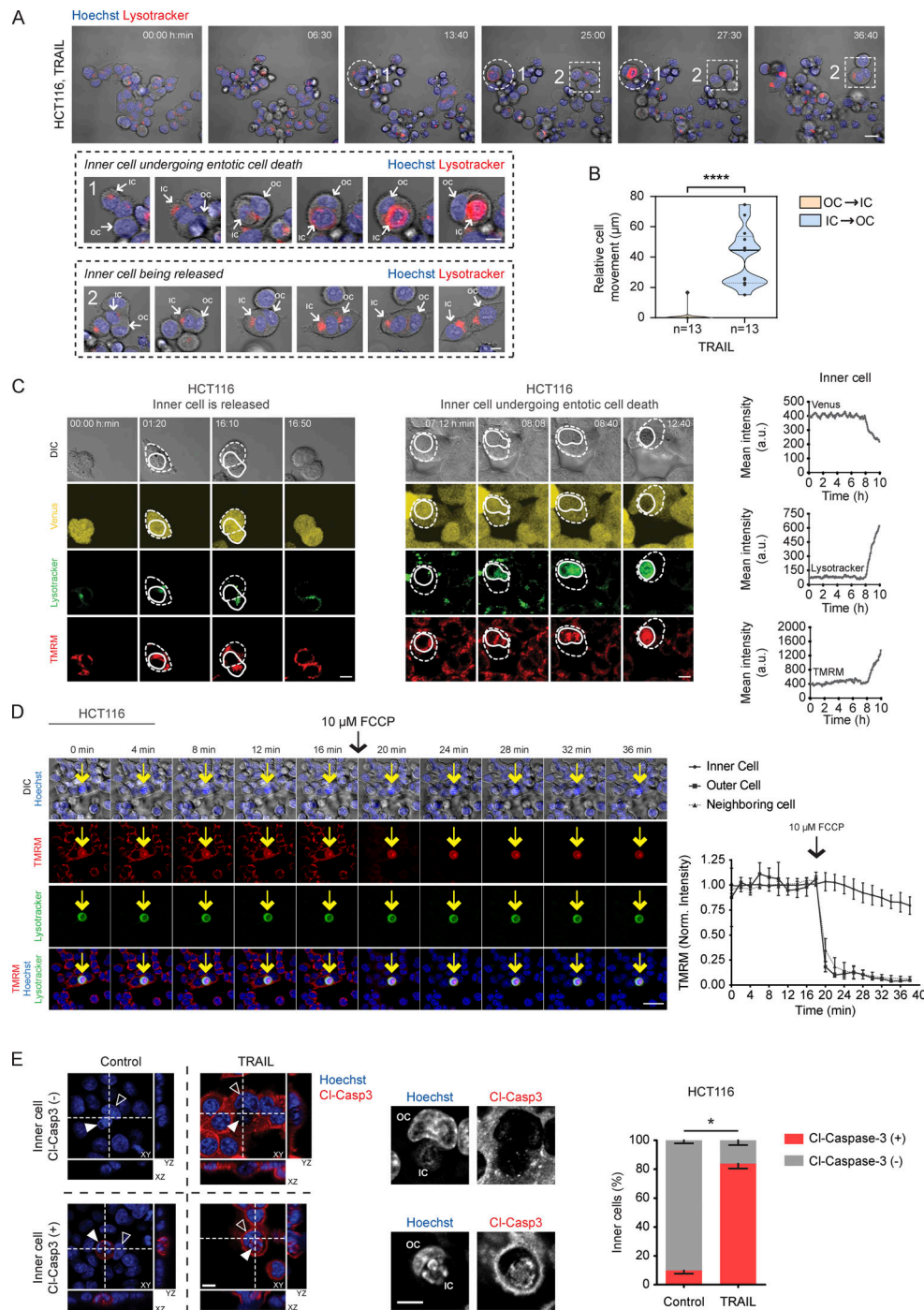


Figure S1. **Long-term time-lapse microscopy verifies induction of entotic structures by TRAIL treatment.** (A) Representative time-lapse images of Hoechst and LysoTracker staining in HCT116 cells showing formation of entotic structures in TRAIL treatment. Representative entosis events of an inner cell undergoing entotic cell death (1) and an inner cell being released (2) are highlighted. Formation and stages of depicted entosis events are shown. Inner cells and outer cells are highlighted with white arrows. (B) Quantification of relative cell movement of inner and outer cells in TRAIL-treated HCT116 cells. Thirteen entotic structures per group from three experiments were monitored by time-lapse microscopy. Data are shown as individual values for each cell as well as median and quartiles. ****, $P < 0.0001$ by unpaired two-tailed t test. (C) Representative time-lapse images of DIC, Venus, LysoTracker, and TMRM showing an inner cell being released (left) and inner cell undergoing entotic cell death (right). Accumulation of TMRM and LysoTracker coincides with the loss of Venus signal in the entotic inner cell (right). Solid and dashed lines indicate inner and outer cells, respectively. Scale bar: 20 μm . (D) Representative time-lapse images of DIC, Hoechst, TMRM, and LysoTracker showing the effects of FCCP treatment on inner cell TMRM signal during entotic cell death. Quantification of TMRM mean fluorescence intensity in the corresponding inner, outer, and neighboring cells. Yellow arrows indicate inner cell. Scale bar: 20 μm . (E) Representative 3D confocal microscopy images of Hoechst (blue) and cleaved caspase-3 (Cl-Casp3; red) staining showing Cl-Casp3-positive and Cl-Casp3-negative inner cells in control and TRAIL-treated cells. Quantification of inner cell Cl-Casp3 status in control and TRAIL-treated cells. White and black arrowheads indicate inner and outer cells, respectively. Scale bar: 20 μm . Data are shown as mean \pm SEM from three experiments. *, $P < 0.05$ by unpaired two-tailed t test. IC, inner cell; Norm., normalized; OC, outer cell.

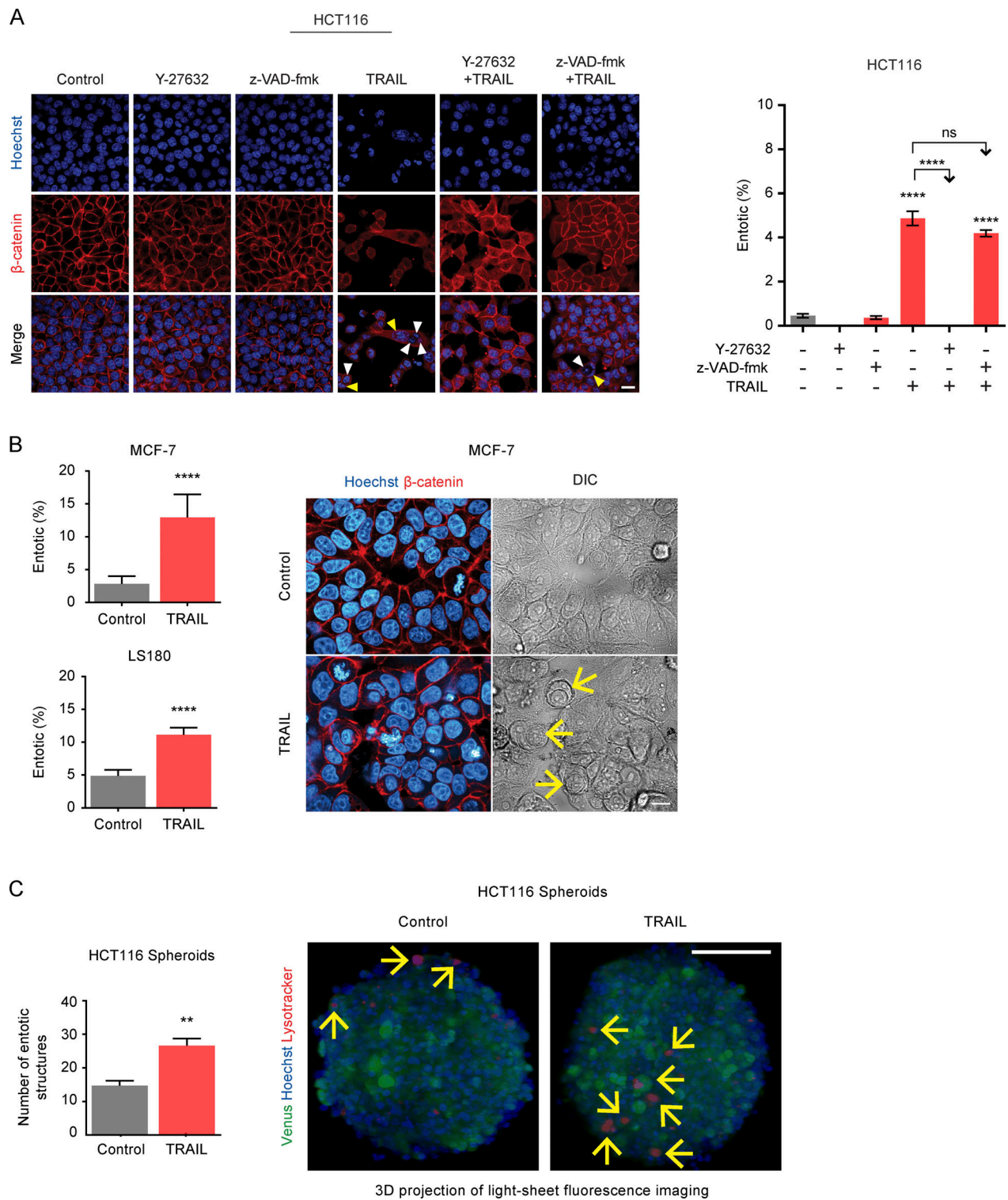


Figure S2. **Representative images and manual quantification of entotic structures in HCT116, MCF-7, and LS180 cells as well as HCT116 spheroids with or without TRAIL treatment.** (A) Representative confocal microscopy images of Hoechst (blue) and β -catenin (red) staining and quantification of entotic structures in HCT116 cells treated with or without TRAIL in the absence or presence of z-VAD-fmk or Y-27632. More than 500 cells were manually quantified from at least two experiments. White and yellow arrowheads indicate inner and outer cells, respectively. Scale bar: 20 μ m. (B) Quantification of entotic events in MCF-7 and LS180 cells treated with or without TRAIL. Representative confocal microscopy images of DIC, Hoechst (blue), and β -catenin (red) staining in MCF-7 cells treated with control or TRAIL are shown. Yellow arrows indicate entosis events. More than 500 cells were quantified from at least two experiments. Scale bar: 20 μ m. (C) Quantification of entotic events in HCT116 spheroids treated with control or TRAIL (left). 3D projections of light sheet fluorescence imaging of Venus (green), Hoechst (blue), and LysoTracker (red) in control and TRAIL-treated HCT116 spheroids. Three spheroids per treatment were quantified. Yellow arrows indicate LysoTracker-positive inner cells. Scale bar: 100 μ m. Data are shown as mean \pm SD. **, $P < 0.01$; ***, $P < 0.0001$ by unpaired two-tailed t test.

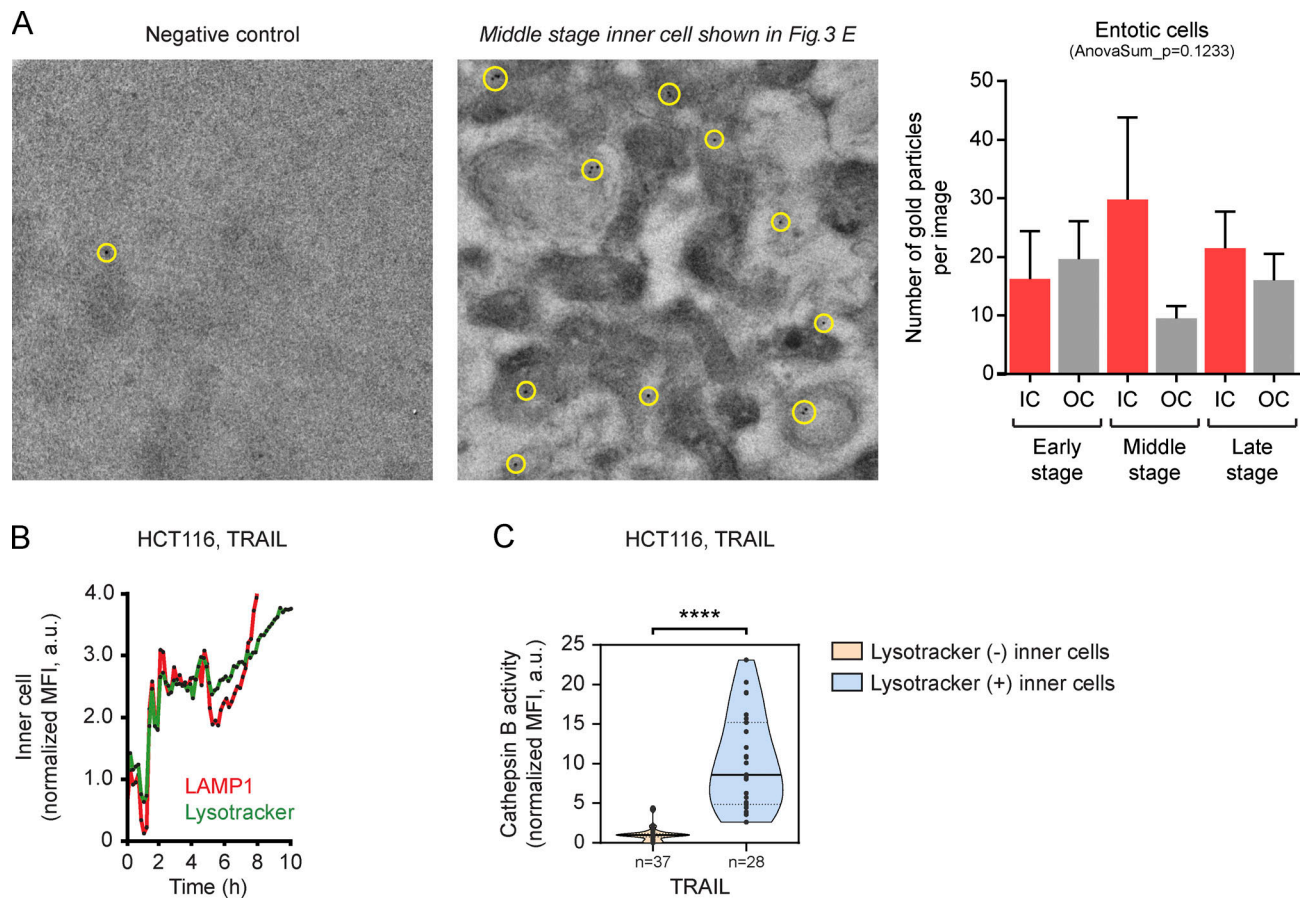


Figure S3. **Ultrastructural localization of LC3 in negative control and middle-stage inner cell shown in Fig. 3. (A)** Representative TEM images showing ultrastructural localization of LC3 in negative control and middle-stage inner cell shown in Fig. 3 D. Yellow circles indicate gold particles. Quantification of gold particles in early-, middle-, and late-stage inner and outer cells shown in Fig. 3. Statistical significance was tested using one-way ANOVA followed by Tukey's multiple comparison test. **(B)** Quantification of LAMP1 and LysoTracker mean fluorescence intensity (MFI) in depicted inner cell undergoing entotic cell death shown in Fig. 3 F. **(C)** Quantification of cathepsin B activity in early- and late-stage entotic cells corresponding to Fig. 3 G. $n = 37$ (early stage) and $n = 28$ (late stage) inner cells were quantified from three experiments. Data are shown as individual values for each cell as well as median and quartiles. ****, $P < 0.0001$ by unpaired two-tailed t test. IC, inner cell; OC, outer cell.

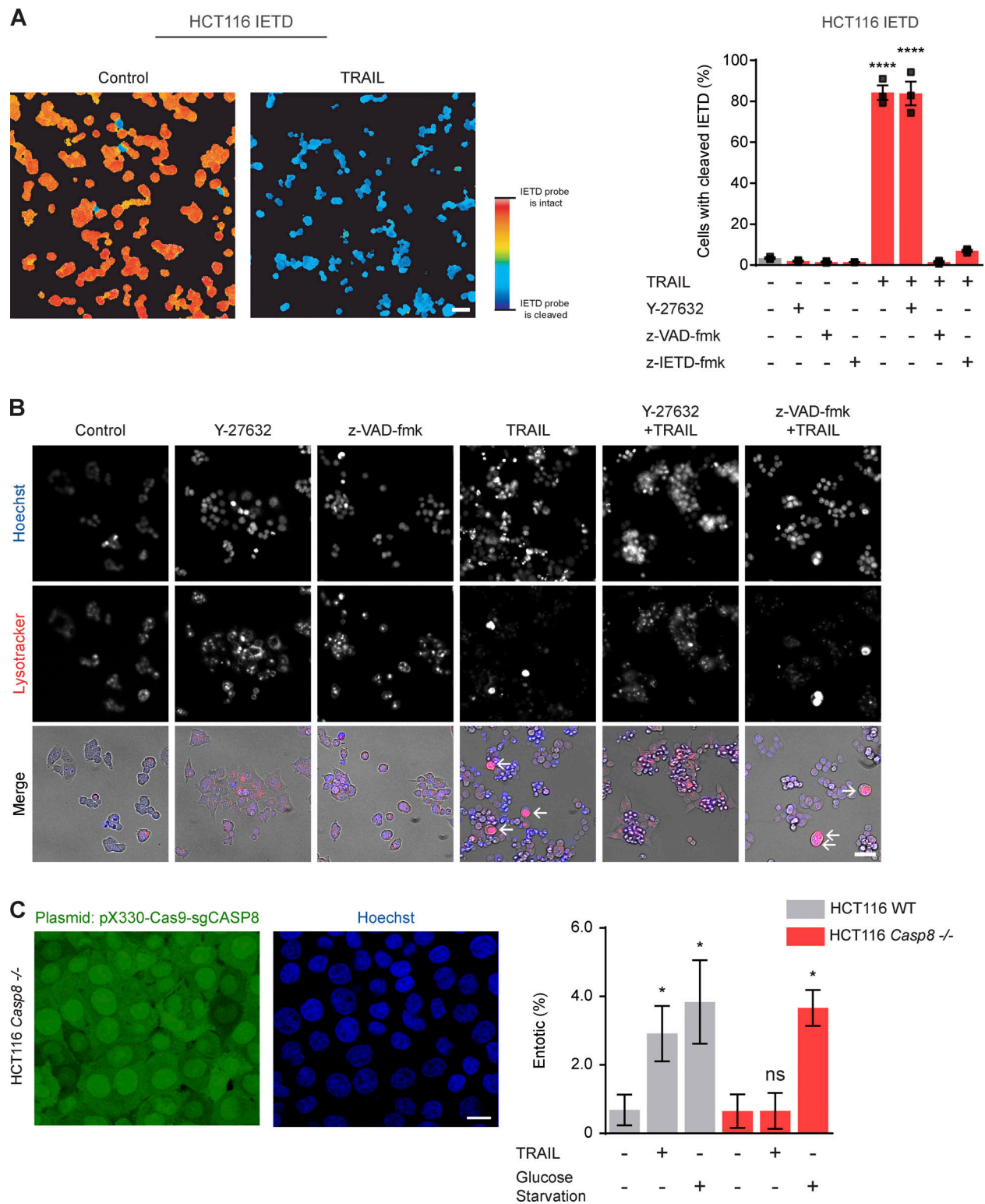


Figure S4. **Representative fields of view and quantification of cells with cleaved IETD substrate in HCT116 cells treated with or without TRAIL in the absence or presence of Y-27632 or caspase inhibitors. (A)** Representative images and quantification of cells with cleaved IETD substrate in HCT116 cells treated with or without TRAIL in the absence or presence of z-VAD-fmk, z-IETD-fmk, or Y-27632. Scale bar: 25 μ m. Data are shown as individual values for each experiment as well as mean \pm SEM from three experiments. ****, $P < 0.0001$ by one-way ANOVA followed by Tukey's multiple comparison test. **(B)** Representative images of Hoechst and LysoTracker staining in HCT116 cells treated with or without TRAIL in the absence or presence of z-VAD-fmk or Y-27632. Arrows indicate entosis events. Scale bar: 25 μ m. **(C)** Representative images of Hoechst-stained (blue) HCT116 CASP8^{-/-} cells (pX330-Cas9-sgCASP8; green). Quantification of entotic events in control, TRAIL-treated, or glucose-starved HCT116 WT and CASP8^{-/-} cells. More than 500 cells were manually quantified from two experiments. Scale bar: 20 μ m. Data are shown as mean \pm SD. *, $P < 0.05$ by one-way ANOVA followed by Tukey's multiple comparison test.

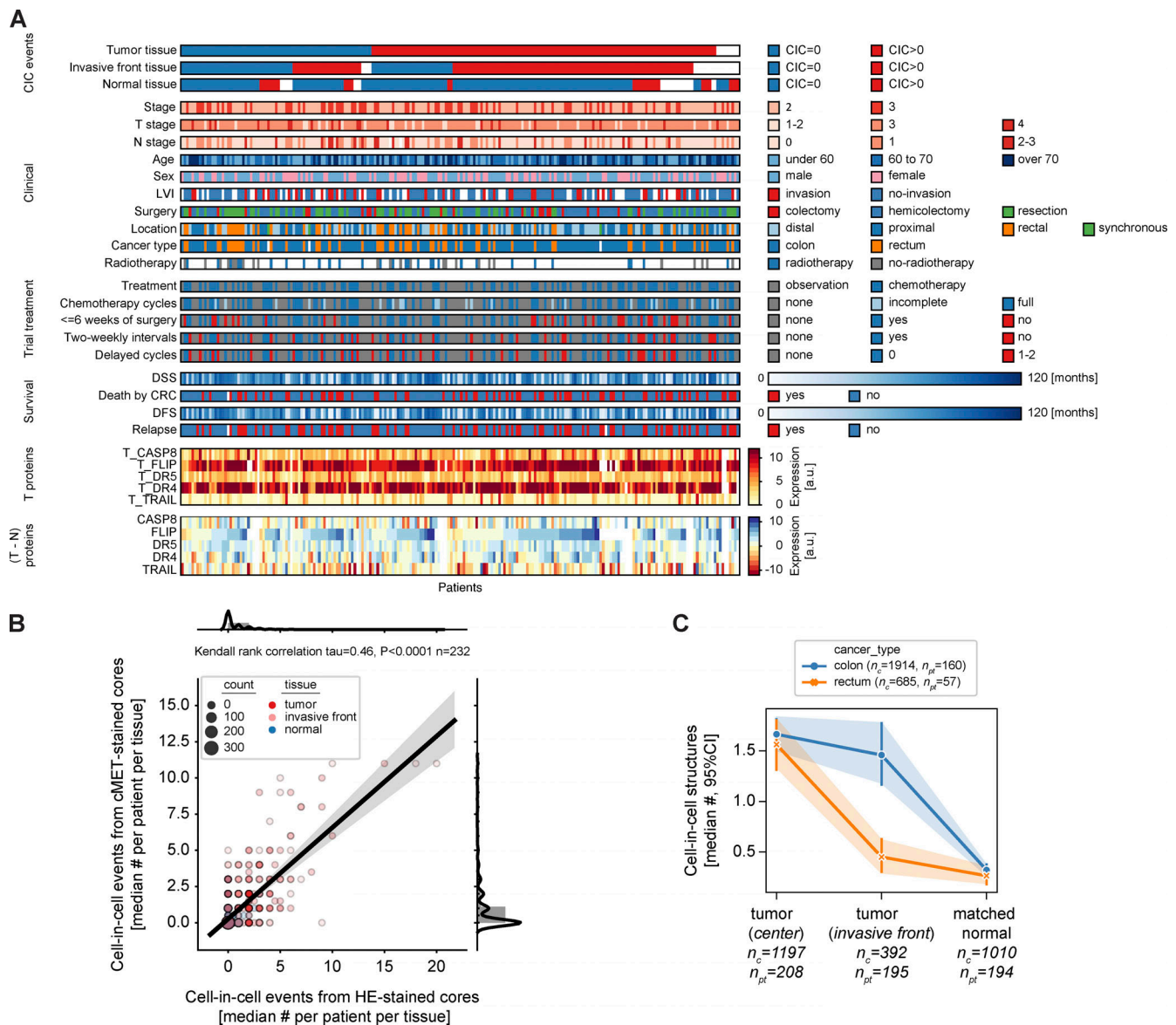


Figure S5. **Overview of clinical, demographic, pathological, and molecular information for the CRC patients of the N1240 phase III clinical trial.** **(A)** Each column represents a patient and each row color codes a feature. Missing data are shown in white. CIC-derived features include estimates of absence (CIC = 0) or presence (CIC > 0) of CIC events from TMA sections prepared from tumor, invasive front, and normal tissue. Visualization was generated with the MATLAB package HCP. **(B)** Comparison between CIC events (median aggregated by patient, tissue, and staining marker) observed in TMA sections stained for H&E and c-MET. Marker color indicates tissue type. Marker size and transparency encode the number of cores. Solid black line and gray shaded area indicate the regression line and CI, respectively. Agreement between CIC estimates from H&E-stained and c-MET-stained TMA cores was computed using the Kendall τ correlation (Python package scipy). **(C)** CIC events (median and 95% CI) detected in TMA sections prepared from tumor center, invasive front, and matched normal tissue of colon or rectum. n_c and n_{pt} indicate number of tumor cores and patients, respectively. LVI, lymphovascular invasion.

Video 1. **HCT116 IETD cells showing formation of apoptotic and entotic structures in response to TRAIL treatment.** TMRM and Venus are pseudo-colored as red and green. Arrowheads indicate entotic structures. Frame rate: 20 frames/second. Corresponds to Fig. 1, G and H.

Video 2. **HCT116 cells showing surviving and dying entotic cells in response to TRAIL treatment.** Arrowheads indicate entotic structures. Merge of DIC, Hoechst (blue), and LysoTracker (red) is shown. Frame rate: 15 frames/second. Corresponds to [Fig. S1 A](#).

Video 3. **3D projection of an inner cell showing LysoTracker (red) accumulation during entosis.** Hoechst and MitoTracker are pseudocolored as blue and green. Frame rate: 15 frames/second.

Video 4. **Reduction of Venus (yellow) signal coincides with accumulation of TMRM (red) and LysoTracker (green) in inner cells during entotic cell death.** Frame rate: 20 frames/second. Corresponds to [Fig. S1 C](#).

Video 5. **3D projection of HCT116 IETD spheroids showing entotic structures in control and TRAIL treatment.** Venus (green), Hoechst (blue), and LysoTracker (red) are presented. LysoTracker-stained nuclei indicate late-stage entotic cells. Frame rate: 30 frames/second. Corresponds to [Fig. S2 C](#).

Video 6. **Lysosomal events during entotic cell death in TRAIL-treated cells.** HCT116 cells transfected with LAMP1-mscarlet-1 (red) and stained with Hoechst (blue) and LysoTracker (green). Frame rate: 8 frames/second. Corresponds to [Fig. 3 F](#).

Video 7. **Release of inner cells in HCT116 *Bax*^{-/-} *Bak*^{-/-} during TRAIL treatment.** Arrowheads indicate inner cells. Frame rate: 15 frames/second. Corresponds to [Fig. 5](#).